Thermodynamic Processes Driving Thermal Circulations on Slopes: Modeling Anabatic and Katabatic Flows on Reunion Island

Samira El gdachi, Pierre Tulet, Anne Réchou, Frédéric Burnet, C Mouchel-vallon, C. Jambert, M. Leriche

JGR Atmospheres

RESEARCH ARTICLE
10.1029/2023JD040431

Thermodynamic Processes Driving Thermal Circulations on Slopes: Modeling Anabatic and Katabatic Flows on Reunion Island

S. El Gdachi[1], P. Tulet[2], A. Réchou[1], F. Burnet[3], C. Mouchel-Vallon[2], C. Jambert[2], and M. Leriche[4,5]

[1]Laboratoire de l'Atmosphère et des Cyclones (LACy), UMR 8105, Université de la Réunion, Saint-Denis, France, [2]Laboratoire d'Aérologie (LAERO), UMR 5560, CNRS, UT3, IRD, Toulouse, France, [3]Centre National de Recherches Météorologiques (CNRM), UMR 3589, CNRS, Université de Toulouse, Toulouse, France, [4]Laboratoire de Météorologie Physique (LaMP), UMR 6016, CNRS, Université Clermont Auvergne, Aubière, France, [5]Département des Sciences de la Terre et de L'atmosphère, Centre Pour l'étude et la Simulation du Climat à L'échelle Régionale (ESCER), Université du Québec à Montréal, Montréal, QC, Canada

Abstract This study investigates thermal circulations on Reunion Island (21°07'S 55°32'E), focusing on the complex terrain of the region. Observations from the BIO-MAÏDO campaign, along with 2 days of high-resolution simulation using the MesoNH model, were analyzed to understand the thermally-driven mechanisms. This simulation was conducted with a horizontal resolution of 100 m and employed a vertically stretched grid, achieving a resolution of 1 m at the lowest levels. Two distinct wind regimes were identified, characterized by katabatic flows prevailing within a 30 m thick layer during nighttime, and an anabatic flow manifesting within a layer spanning from 150 to 200 m during the daytime. The simulation was confirmed through validation with surface measurements, and thus enabling a detailed study of thermal breeze circulations. Results reveal that the intensity of trade winds significantly influences the development of thermal circulations. Complex layered structures in the atmosphere were also identified. At an intensity of 7 m s^{-1}, trade winds impede the development of thermal circulations atop the slope, and result in the emergence of a convergence zone between local and regional circulations. The analysis of the breeze establishment period indicates that the katabatic flow stabilizes in 35 min, quicker than the anabatic flow, which takes 110 min. Momentum and heat budget analysis provide insights into the primary drivers of thermal circulations: buoyancy acceleration, influenced by local surface heating during anabatic flow onset, and local surface cooling during katabatic flow onset.

Plain Language Summary This research explores thermal circulation in the northwestern region of Reunion Island, an area significantly influenced by the return flow of the trade winds, the trade winds themselves, and breezes. Data from the BIOMAÏDO campaign and simulation using the MesoNH model were employed to analyze the heat-driven air movements in this specific region. The study identified two distinct wind patterns: a downward katabatic flow within a 30 m layer and a diurnal anabatic flow occurring between elevetions of 150–200 m. Validation through surface measurements corroborated the model simulation, facilitating a detailed analysis of thermal breeze circulations. The results indicate that strong directional winds significantly influence air movement patterns. At a speed of 7 m s^{-1}, these winds inhibit upward air movement along the slopes, creating a convergence zone between local and larger-scale wind patterns. Analysis of the breeze establishment periods indicated a faster stabilization of katabatic flow at 35 min compared to 110 min of anabatic flow. Momentum and heat budget analysis revealed the primary drivers: buoyancy acceleration, influenced by local surface heating during anabatic flow and by local surface cooling during katabatic flow.

Key Points:

- Trade winds strongly impact thermal circulations on Reunion Island, creating complex atmospheric structures
- Katabatic flow stabilizes faster (35 min) than anabatic flow (110 min), affecting the island's thermal breeze patterns
- Buoyancy acceleration, local surface heating, and cooling play significant roles in driving thermal circulations

Correspondence to:
P. Tulet and S. El Gdachi,
pierre.tulet@cnrs.fr;
samira.el-gdachi@univ-reunion.fr

Citation:
El Gdachi, S., Tulet, P., Réchou, A., Burnet, F., Mouchel-Vallon, C., Jambert, C., & Leriche, M. (2024). Thermodynamic processes driving thermal circulations on slopes: Modeling anabatic and katabatic flows on Reunion Island. *Journal of Geophysical Research: Atmospheres*, *129*, e2023JD040431. https://doi.org/10.1029/2023JD040431

Received 16 NOV 2023
Accepted 15 AUG 2024

Author Contributions:
Conceptualization: S. El Gdachi, P. Tulet, A. Réchou
Data curation: S. El Gdachi, P. Tulet, A. Réchou
Formal analysis: S. El Gdachi, P. Tulet, A. Réchou, F. Burnet, C. Mouchel-Vallon, C. Jambert, M. Leriche
Funding acquisition: P. Tulet, M. Leriche
Investigation: S. El Gdachi, P. Tulet, A. Réchou
Methodology: S. El Gdachi, P. Tulet, A. Réchou
Project administration: P. Tulet, M. Leriche
Resources: P. Tulet, M. Leriche
Software: S. El Gdachi, P. Tulet
Supervision: P. Tulet, A. Réchou

1. Introduction

Understanding thermal circulations is important for improving weather and air quality forecasting (Chemel et al., 2016; Sabatier et al., 2020). These local wind systems, known as thermal breezes, are generated over coastal regions (sea/land breeze) or mountainous terrain (valley/mountain breeze) due to the buoyancy effects caused by the heating and cooling of the lower atmospheric layer during the diurnal cycle. Slope breezes cause the air to rise during the day (anabatic) and descend at night (katabatic). Research on the behavior of thermal breezes over mountainous islands has been ongoing for several decades (Zardi & Whiteman, 2013). For example, over the Hawaiian islands of Kauai and Oahu, trade winds can surmount the 1,000–1,500 m terrain crests (Wang &

Validation: S. El Gdachi, P. Tulet, A. Réchou, F. Burnet, C. Jambert, M. Leriche
Visualization: S. El Gdachi, P. Tulet, A. Réchou
Writing – original draft: S. El Gdachi, P. Tulet, A. Réchou, F. Burnet, C. Mouchel-Vallon, C. Jambert, M. Leriche
Writing – review & editing: S. El Gdachi, P. Tulet, A. Réchou

Kirshbaum, 2015). Additionally, the presence of a trade wind inversion for exemple at Maui County, Hawaii, impacts the circulations above these areas (Carlis et al., 2010). Studying these phenomena over slopes remains challenging due to frequent, significant, and localized air mass changes (Sturman & McGowan, 1995), resulting from the interaction between regional air masses and local processes (Lesouëf et al., 2011), which cannot be generalized across different valleys (Duine et al., 2017; Giovannini et al., 2017; Rucker et al., 2008).

Numerical simulations have become an essential tool for understanding the complex atmospheric processes involved in the local wind flows around islands and mountainous terrains. Studies aim to find optimal configurations for simulating these phenomena. Sensitivity tests show that improvements in simulated ground temperature, land–sea thermal contrast, and mixing ratio enhance the simulation of land/sea breeze strength (Yang et al., 2005). However, another critical factor that can greatly impact the quality and accuracy of the results is the choice of resolution. Cécé et al. (2014) used numerical simulations to examine island-induced circulations and windward katabatic flow over the Guadeloupe Archipelago. While the study provided valuable insights into the impact of islands on local wind flows, the effect of the atmosphere's lower layer on the formation and sustainment/destruction of wind fronts in three-dimensional scenarios during daytime is still not completely understood.

Using a horizontal resolution of 1 km on steep terrain such as the Guadeloupe Archipelago can smooth out the topography. Therefore, a better option would be to use high-resolution mesoscale simulations of about 100 m horizontal grid lengths (Cuxart, 2015) which proved to be a good compromise between large-eddy simulations and mesoscale simulations. These high-resolution simulations can capture valleys and thermally driven flows.

Similarly, Cuxart et al. (2014) showed that the use of high vertical resolution such as 3 m and detailed characterization of the land surface, with horizontal resolution of 1 km, can provide valuable insights into near surface processes like sea breezes. In this study, Cuxart et al. (2014) employed a comprehensive approach for investigating the processes responsible for thermal circulations, using thermodynamic budgets to analyze sea breeze phenomena. The study utilized momentum, temperature, and turbulence kinetic energy budgets obtained from a numerical model to describe the spatiotemporal structure of sea breezes over the island of Mallorca, Spain. By analyzing the evolution of sea breezes in five stages, from before dawn to after sunset, the study identified the dominant physical mechanisms driving sea breeze formation and propagation. Notably, the study revealed that the sea breeze below 200 m MSL is primarily governed by the balance between both the pressure gradient and turbulence which both decrease in intensity during the afternoon.

Recently, a study on the Arve River valley near Mont Blanc (Sabatier et al., 2020) and an investigation on the vertical heat and moisture exchange in the convective boundary layer over mountainous terrain (Weinkaemmerer et al., 2022) both demonstrated the significance of local flow structure and circulation in mountainous regions. While Sabatier's study focused on the impact of thermal stratification, radiative forcing, and snow cover on the flow structure and pollutant distribution, Weinkaemmerer et al. (2022) examined the importance of thermal upslope winds for moisture export from the valley to the mountain tops. Both studies highlight the importance of tributary valleys on daytime and nighttime dynamics and the significant contribution of thermal circulation to vertical transport. These findings also emphasize the importance of using high-resolution numerical simulations. Sabatier et al. (2020) used a semi-idealized framework with a vertical resolution of 2 m as recommended by Blein (2016) and a horizontal resolution of 100 m, while Weinkaemmerer used a grid of 40 m horizontally and 8 m vertically to simulate a more realistic experiment that included a full diurnal cycle with radiation forcing and an interactive land surface model.

In another study, Tian and Miao (2019) demonstrated the crucial role that turbulent transport plays in the development and transition of breeze circulation in mountainous plains of eastern Chengdu (China). This conclusion was reached through an analysis of turbulent fluxes of heat, humidity, and momentum, utilizing nested simulations with the resolutions of 27, 9, 3, and 1, and 35 km vertical levels, 24 of which are below 2 km.

Reunion Island, located in the Indian Ocean at 21°07'S and 55°32'E (Figure 1), is a young volcanic island covering an area of 2,512 km^2, featuring a wide variety of reliefs. The island is formed by two major volcanic areas: the extinct Piton des Neiges and the active Piton de la Fournaise. The rugged terrain includes three notable cirques (Mafate, Salazie, and Cilaos) created by the collapse of Piton des Neiges. The island's diverse and rugged terrain provides an ideal natural setting for studying these thermal circulations. Previous research studies by Lesouëf (2010), Durand et al. (2014), Tulet et al. (2017), Foucart et al. (2018), and Réchou et al. (2019) have extensively investigated the meteorological circulations on the island. The southeast trade winds dominate the

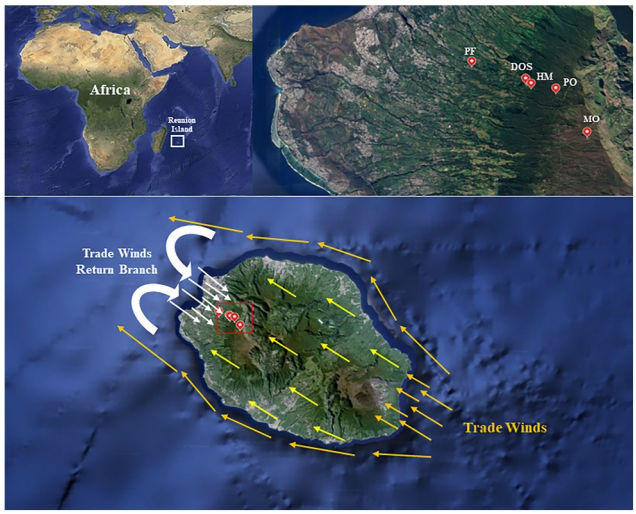

Figure 1. Map of Reunion Island, including locations of the equipped sites deployed during the BIO-MAÏDO campaign. PF (965 m) for Petite France, DOS (1,465 m) for Domaine des Orchidées Sauvages, HM (1,500 m) for Hôtel du Maïdo, PO (1,760 m) for Piste Oméga and MO (2,165 m) for Observatoire du Maïdo. Local atmospheric dynamic pattern represented in arrows around the island.

island's climate as illustrated in Figure 1, with strong winds occurring during the winter season (June–August) and moderate to weak winds during the summer months (December to February). As a result, the southeast, northeast and southwest edges of the island are particularly affected by these trade winds, while a northwesterly leeward circulation occurs in the northwest of the island (e.g., Maïdo area). The circulations over the terrain at the scale of Reunion island are modeled. Although these circulations are not detailed here, they play a significant role in the organization of the local dynamics, particularly due to the highly rugged terrain. The slopes of the Maïdo area experience sea and valley breezes, which advect the oceanic air masses and induce convection on the mountain slopes. Duflot et al. (2019) demonstrated that this convection leads to the formation of clouds almost daily, which are typically shallow and contain low amounts of water. Given the complex topography and unique meteorological conditions of Reunion Island, further investigation of thermal circulations is crucial to develop a more comprehensive understanding of the island's climate and provide better weather forecasts. The detailed analysis of thermal circulations, especially in the Maïdo area, can provide insight into the formation of clouds and precipitation.

The purpose of this paper is to investigate the drivers and impacts of thermal and dynamic circulations over Reunion Island. Data collected during the BIO-MAÏDO campaign (Bio-physicochemistry of tropical clouds at Maïdo, Reunion Island; https://bio-ma"{i}do.aeris-data.fr/), which took place from 11 March to 7 April 2019 (Leriche et al., 2023), serve as a basis for this investigation. MesoNH, a non-hydrostatic atmospheric model co-developed by Laboratoire d'Aérologie (LAERO, UMR 5560 UPS/CNRS) and Center National de Recherches Météorologiques (CNRM, UMR 3589 CNRS/Météo-France; http://mesonh.aero.obs-mip.fr/; (Lac et al., 2018)), is used for high-resolution numerical simulation. Our goal is to analyze the specific local-scale phenomenon within the complex terrain of Reunion Island using high-resolution simulation.

The article is structured as follows. Section 2 introduces the research topic of thermally-driven circulation patterns over Reunion Island, the BIO-MAÏDO campaign, and the MesoNH model and its configuration. Section 3 examines an overview of the BIO-MAÏDO campaign results and compares model simulation with surface observations and data collected from a tethered balloon. Section 4 analyzes circulation patterns over Reunion Island, including those over the Maïdo region and along the slope. Section 5 investigates the main terms in the budgets of potential temperature and momentum budget profiles and along the slope, as well as the time series of these budgets. Finally, some conclusions are presented.

2. Methodology

2.1. The BIO-MAÏDO Campaign

The BIO-MAÏDO campaign had several goals including characterizing the dynamics and the evolution of the boundary layer, studying the macro and micro-physical properties of clouds, investigating the chemical and biological composition of the air mass, and understanding the formation processes of secondary organic matter in heterogeneous environments.

Five measurement sites were located along the mountain slope at different altitudes (Figure 1):

- Site 1 named Petite-France (PF, 965 m, 21°2′33″S 55°19′32″E) is located in a sparsely populated area. Its strategic location allows for the characterization of air masses influenced by coastal urbanization and marine air masses that ascend the slope during the day. The site is typically located below the cloud base and is mainly impacted by marine and anthropogenic emissions. To this end, it has been instrumented to characterize the gaseous and particulate chemical composition of the air masses. Additionally, the site is equipped with a ceilometer to enable the characterization of the boundary layer evolution and the cloud cycle.
- Site 2 named Domaine des Orchidées Sauvages (DOS, 1,465 m, 21°3′7″S 55°21′11″E) is a rural site composed of diverse vegetation including trees, meadows, and crops. Its location on the Maido slope provides

an ideal opportunity to measure the life cycle of slope clouds. DOS is instrumented with a tethered balloon, a meteorological station, complementary probes monitoring the size spectrum of particles, a present weather visibility sensor associated with a droplet size spectrometer to characterize the microphysical properties of clouds, as well as a ceilometer.

- Site 3 named Hôtel du Maïdo (HM, 1,500 m, 21°3′16″S 55°21′21″E) is located in an environment mainly composed of diverse trees (such as tamarinds) and is relatively distant from anthropogenic emissions. The site is designed to measure turbulent fluxes (enthalpy and trace gases) in forested environments. HM is instrumented with a 24 m mast and a container that allows for volatile organic compounds (VOC) flux measurements. The mast is equipped with a sonic anemometer and an analyzer of carbon dioxide and water vapor, while a pump inside the container is connected to an inlet installed at the top of the mast to transport air to several devices for analysis.
- Site 4 named Piste Oméga (PO, 1760 m, 21°3′26″S 55°22′5″E) is located in a forested area mainly composed of tamarinds and is far from anthropogenic sources. Its altitude corresponds to the sectors where slope clouds regularly come into contact with the ground. The site is equipped with a 10 m mobile mast with a meteorological station, a Cloud drop probe (CDP), an AEROVOCC sampler (AtmosphERic Oxygenated/VOC in Cloud), and a cloud impactor to collect and analyze the chemical composition of cloud droplets.
- Site 5 corresponds to the Observatoire du Maïdo (MO, 2,165 m, 21°4′46″S 55°22′59″E; Baray et al. (2013)). Positioned near the Maïdo crest, above forested areas with a surface consisting of basaltic slabs and shrubs. Notably, this location primarily rests above the cloud level of the slope. The BIO-MAÏDO campaign benefited from observations of aerosols and gases as well as basic meteorological parameters at this site.

In this work, we discuss the circulations based on meteorological data (air temperature, wind speed, and wind direction) at the mid-slope (PF station) and at the top of the slope (MO station). The instrument used to investigate the vertical structure of the atmosphere is the tethered balloon in DOS. It was equipped with many instruments: an ultrasonic anemometer, a high-frequency temperature probe, an Optical particle Counter (OPC), and a CDP. The tethered balloon was maintained to the ground by a cable and can go up to 1 km of altitude. During the campaign, 144 hr of tethered balloon measurements were made in 21 days of operation.

Several studies have already analyzed the data from the campaign, which were used as a basis for selecting the study period. Dominutti et al. (2022) presented the results of their investigation on the characterization of atmospheric aerosols and gases in PF and MO, focusing on the anthropogenic influence, the formation processes of secondary organic aerosols, and the impact of aqueous transformation on the chemical and physical properties of particles. According to Rocco et al. (2022), 6 days have a strong dynamic connection between PF and MO. The highest percentage of connections was observed for 15 March to 16 March and from 28 March to 1 April, with 82% of all trajectories connecting PF to MO. However, the first period of the campaign had limited observations, and there were no tethered balloon flights on 31 March. 28 and 30 March were identified as “golden days” with the highest potential for analyzing dynamic circulations.

2.2. The MesoNH Model

MesoNH (Lac et al., 2018) can be used to simulate atmospheric flows on abrupt topography and is equipped with a complete set of parameterizations to represent various atmospheric physical and chemical processes. The MesoNH model has been used in a variety of investigations from LES (Large-Eddy Simulations) (Cuxart et al., 2000) to the mesoscale (Lafore et al., 1998).

In this study, MesoNH was launched using the two-way nesting method. The simulation has three nested domains (Figure 2); the red squares in Figures 2a and 2b show the location of the second and the third domains. The first domain with high model grid spacing (2 km) covers a 300 × 300 km square centered over Reunion Island. The second domain surrounding Reunion Island represents a 70 × 70 km square with a horizontal model grid spacing of 500 m. The third domain has a 100 m resolution and covers a 12 × 12 km area centered on the observation sites (PF, DOS, HM, PO, MO). The vertical grid common to the 3 domains includes 120 levels of non-linear resolution that follow the relief up to 27 km in altitude (Gal-Chen & Somerville, 1975). The vertical stretching of the model levels has made it possible to increase the resolution near the ground ($\Delta z = 1$ m at the first level), with 59 levels between the surface and 500 m, resulting in a more precise depiction of the atmospheric boundary layer (ABL).

For the largest domain, the 1D turbulence scheme (Randall et al., 1996) is used with a buoyancy-based mixing length based on Bougeault and Lacarrere's parameterization (Bougeault & Lacarrere, 1989). To resolve the

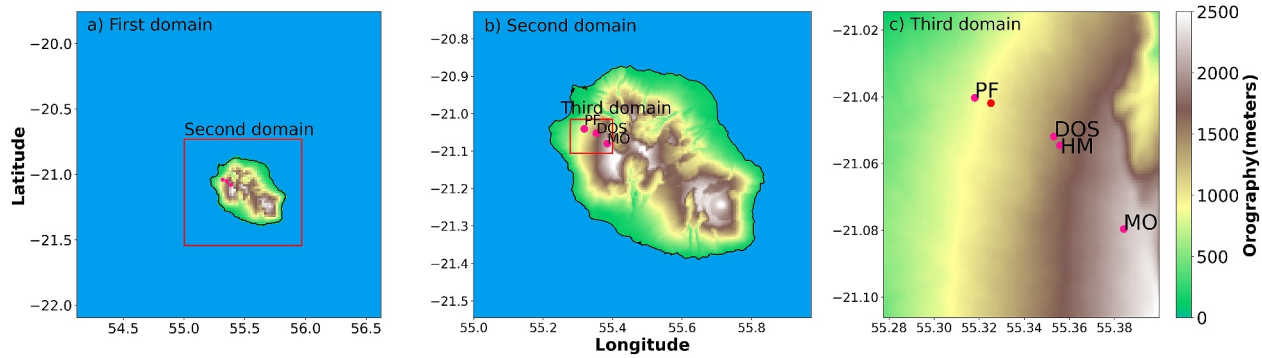

Figure 2. Nested model domains: the color scale represents terrain elevation as seen by the models (m above mean sea level). (a) The first domain (2 km). (b) The second domain (500 m). (c) The third domain (100 m). The location of the measuring stations used for model comparison has been overlaid (pink dot): PF for Petite France, DOS for Domaine des Orchidées Sauvages, HM for Hôtel du Maïdo, and MO for Observatoire du Maïdo.

turbulence eddies of the second and last domain (high horizontal resolution), we use a 3D turbulence scheme (Cuxart et al., 2000). In the third domain the mixing length is given by the horizontal mesh size of the domain (Deardorff, 1974). Momentum is transported with the WENO advection scheme (Jiang & Shu, 1996) in the first (2 km) and second domains (500 m). However, the WENO scheme is very diffusive and may filter the resolved vortices. Therefore, for the third domain (100 m), a 4th-order-centered advection scheme (Lunet et al., 2017) was used with a Runge-Kutta 4th-order-centered temporal scheme for momentum advection. The Piecewise Parabolic Method (PPM; (Colella & Woodward, 1984)) was used for meteorological and scalar variable advection with time-splitting handled using the Runge-Kutta 5 steps 3rd order (Lunet et al., 2017). The model also includes coupling with the ISBA land surface scheme (Interaction between Soil Biosphere and Atmosphere; (Noilhan & Planton, 1989)) included in the SURFEX scheme (Masson et al., 2013) for computing surface fluxes. The two-moment microphysical scheme LIMA (Liquid Ice Multiple Aerosol; (Vié et al., 2016)) is chosen to represent the clouds and precipitation life cycle. The lateral boundary conditions were constrained every 6 hr with the Integrated Forecasting System IFS operational HRES analysis from the European Center for Medium-Range Weather Forecasts (https://www.ecmwf.int/en/forecasts).

The detailed characteristics of each domain are listed in Table 1. The simulation started at 18:00 UTC (Local Time is equal to UTC + 4) on 27 March 2019, and ended at 00:00 UTC on 29 March. For the second day, the simulation started at 18:00 UTC on 29 March and ended at 00:00 UTC on 31 March. In each simulation, a 6-hr spin-up was performed to adjust the initial fields to the physical parameterizations and the resolution of the simulation.

Table 1
Overview of MesoNH Model Configurations

Domains	3, Two-ways nested
First domain	128*128 Grid points (2 * 2 km)
Second domain	200*180 Grid points (500 * 500 m)
Third domain	100*127 Grid points (100 * 100 m)
Vertical resolution	Near the ground: $\Delta z = 1$ m; at $z = 500$ m: $\Delta z = 30$ m; top of the domain: $\Delta z = 380$ m
Lateral boundary conditions	Analysis from the ECMWF every 6 hr
Advection schema	
First ans second domain	Weighted essentially non oscillatory
Third domain	The centred schemes fourth order
Microphysical Scheme	The 2-moment mixed-phase microphysical scheme LIMA

2.3. The Budget Equations

The analysis of a trend equation's budget is frequently used in numerical studies to measure different physical processes. It represents the storage or tendency of a physical parameter, in order to understand the physical process underlying. To study the mechanisms responsible for the onset of thermal circulations on slopes, the two-dimensional simplified budgets of slope-parallel momentum and virtual potential temperature (Manins & Sawford, 1979) were examined. The slope-parallel momentum budget is defined in Equation 1:

$$\underbrace{\frac{\partial \overline{u_s}}{\partial t}}_{\text{I}} + \underbrace{\overline{u_s}\frac{\partial \overline{u_s}}{\partial s}}_{\text{II}} + \underbrace{\frac{1}{\rho}\frac{\partial \overline{p}}{\partial s}}_{\text{III}} - \underbrace{g\frac{\overline{d}\sin\beta}{\overline{\theta_{va}}}}_{\text{IV}} + \underbrace{\frac{\partial \overline{u_s' w_n'}}{\partial n}}_{\text{V}} = 0 \quad (1)$$

Where s and n are the slope-parallel and slope-normal coordinates in accordance with the double-rotation of the axes; t is time. u_s and w_n are the wind components of the velocity field in each direction. The term I represents momentum storage. The term II represents horizontal advection and is given by the expression $u_s \frac{\partial u_s}{\partial s}$, where $\frac{\partial u_s}{\partial s}$ is the spatial gradient of u_s in the s-direction.

The term *III* is the along-slope pressure gradient and is given by $\frac{1}{\rho}\frac{\partial p}{\partial s}$, where $\frac{\partial p}{\partial s}$ is the spatial gradient of p in the s-direction and ρ is the air density. The term *IV* is given by $\left(g\frac{\overline{d}\sin\beta}{\overline{\theta_{va}}}\right)$, and it represents buoyancy acceleration, where $g = 9.81$ m s^{-2} is gravity acceleration, $\overline{d} = \overline{\theta_v} - \overline{\theta_{va}}$ is the temperature deficit defined as the difference between the local and unperturbed air virtual potential temperature v_a, and the range of values obtained along the slope (8.5°–9.2°) represents the slope angle α. The term *V* represents the momentum-turbulent-flux divergence. It is given by the expression $\frac{\partial\left(\overline{u_s' w_n'}\right)}{\partial n}$, which describes the turbulent friction with the spatial gradient of the product of the turbulent along-slope velocity anomaly u_s' with the turbulent normal-slope velocity anomaly w_n'.

The slope-parallel virtual potential temperature is given by Equation 2

$$\underbrace{\frac{\partial\overline{\theta_v}}{\partial t}}_{\text{I}} + \underbrace{\overline{u_s}\frac{\partial\overline{\theta_v}}{\partial s}}_{\text{II}} + \underbrace{\overline{w_s}\frac{\partial\overline{\theta_v}}{\partial n}}_{\text{III}} + \underbrace{\frac{\partial\overline{w_n'\theta_v'}}{\partial n}}_{\text{IV}} + \underbrace{\frac{1}{\bar{\rho}c_p}\frac{\partial\overline{R_n}}{\partial n}}_{\text{V}} = 0 \tag{2}$$

The term *I* represents the storage of heat. The terms *II* and *III* describe advection, which is the explicit transport of virtual potential temperature along the slope by the wind, both horizontally and vertically. This transport is given by the expressions $u_s\frac{\partial\theta_v}{\partial s}$ and $w_s\frac{\partial\theta_v}{\partial n}$, where $\frac{\partial\theta_v}{\partial s}$ and $\frac{\partial\theta_v}{\partial n}$ are the spatial gradients of potential temperature along and perpendicular to the slope, respectively. The term *IV* is the divergence term of turbulent transport of heat. It describes the effect of small-scale eddies on the vertical transport of heat and momentum. It is given by the expression $\frac{\partial\left(w_n'\theta_v'\right)}{\partial n}$, describing the spatial gradient of the product of the turbulent velocity anomaly w_n' with the virtual potential temperature anomaly θ_v' in the perpendicular direction to the slope. The term *V* is the net radiation heat flux divergence, referring to the exchange of heat between the Earth's surface and the atmosphere through electromagnetic radiation. It is given by the expression $\frac{1}{\rho c_p}\frac{\partial R_n}{\partial n}$, where $c_p = 1{,}005$ J kg^{-1} K^{-1} is the specific heat of the air at constant pressure and R_n is the net radiation. The overlying bar is used to indicate a 5 min time averaging and the primes indicate a perturbation from the temporal mean.

3. Observations

3.1. Overview of the BIO-MAÏDO

Daily average variation of observed wind direction and wind speed (m s^{-1}) at 10 m at mid-slope (PF, 965 m) and close to the Maïdo crest (MO, 2,165 m) between 11 March and 7 April 2019 are represented in Figure 3. The observations highlight two distinct periods of wind regimes. During the nighttime period (between 15:00 UTC, i.e., 19:00 LT and 04:00 UTC, i.e., 08:00 LT), the wind regimes are from the east and southeast. This circulation at PF represents katabatic flows with mean wind speeds of 2 to 2.5 m s^{-1}. At MO, the wind patterns are the result of the combination of two distinct circulations, namely the katabatic flow and the trade winds, with wind speed higher than 3 m s^{-1}. Following sunrise, solar radiation starts warming the mountain summit. At PF, the wind direction shifts toward the west, and it takes over an hour (from 04:00 UTC to 05:00 UTC) for the wind to settle into a consistent direction. During this time, wind speeds decrease by over 1.5 m s^{-1}. On the other hand, at MO, the wind direction shift occurs 1 hr later (05:00 UTC) than at PF, with an average advance rate of 1 to 2 m s^{-1}. This can be explained by the distance from the development altitude of the anabatic breeze: the breeze starts at the bottom of the slope and takes tens of minutes to reach the summit. The wind regime at MO is more variable, due to the influence of the trade winds. This has previously been demonstrated by Duflot et al. (2019), who noted that MO is located in a zone of confluence and is affected by both wind circulations - the regime of trade winds and anabatic flow. The shift back to east-southeast wind regimes occurs 1 hr after sunset (15:00 UTC) at both sites. During the transition, wind speeds decrease to 1 at PF and 2.5 m s^{-1} at MO. Once the wind direction has become steady (between 15:00 UTC and 04:00 UTC), it quickly strengthens at both stations.

3.2. Model Comparison With Surface Observations

A comparative analysis of meteorological simulations was conducted using data from 16 stations, categorized by altitude, to validate the model presented in Appendix A. The temporal comparison of 2 m temperature, 10 m wind speed, and direction in PF and MO on 28 and 30 March between the MesoNH simulation results from the 100 m

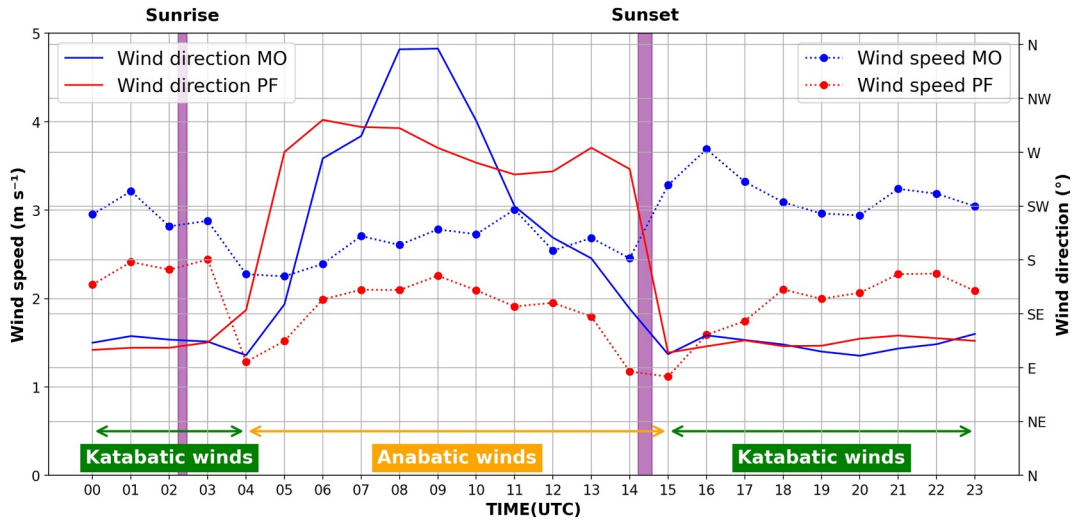

Figure 3. Daily average variation of observed wind direction and wind speed (m s^{-1}) at 10 m at MO and PF over the entire campaign (from 11 March to 7 April).

horizontal resolution domain and the observations are illustrated in Figure 4. On 28 March, after sunrise (02:24 UTC), the temperature increased, reaching a maximum around 09:00 UTC at the MO station with a value of 292.75 K and at the PF station with a maximum of 294.04 K. Although there is a 1 to 2 K temperature discrepancy between the two sites due to the difference in altitude, the MO station 4-d starts to warm 1 hr earlier than the PF station (Figure 4-a). During the 2 days, the simulation reasonably reproduces the hourly 2 m temperature trend. However, it shows a warm bias at PF (~2 K) which reaches 4 K at nighttime compared to observed temperature, potentially due to the heterogeneity of the soil types not represented on a 100 m horizontal resolution of the model. The soil types exhibit higher variability at PF with the presence of a diverse mix of crops, groves, and urban areas whereas in MO it is more homogeneous, featuring primarily brushwood (Leriche et al., 2023). Therefore, this bias is not found in MO. The model displays more accuracy in the MO station with a bias average lower than 0.3 K.

Figures 4-b and 4-e depicts the wind direction on 28 and 30 March for PF and MO stations. At PF (Figure 4-b), the wind direction at night is from the east. After sunrise, the wind direction shifts to the north and northwest and then to

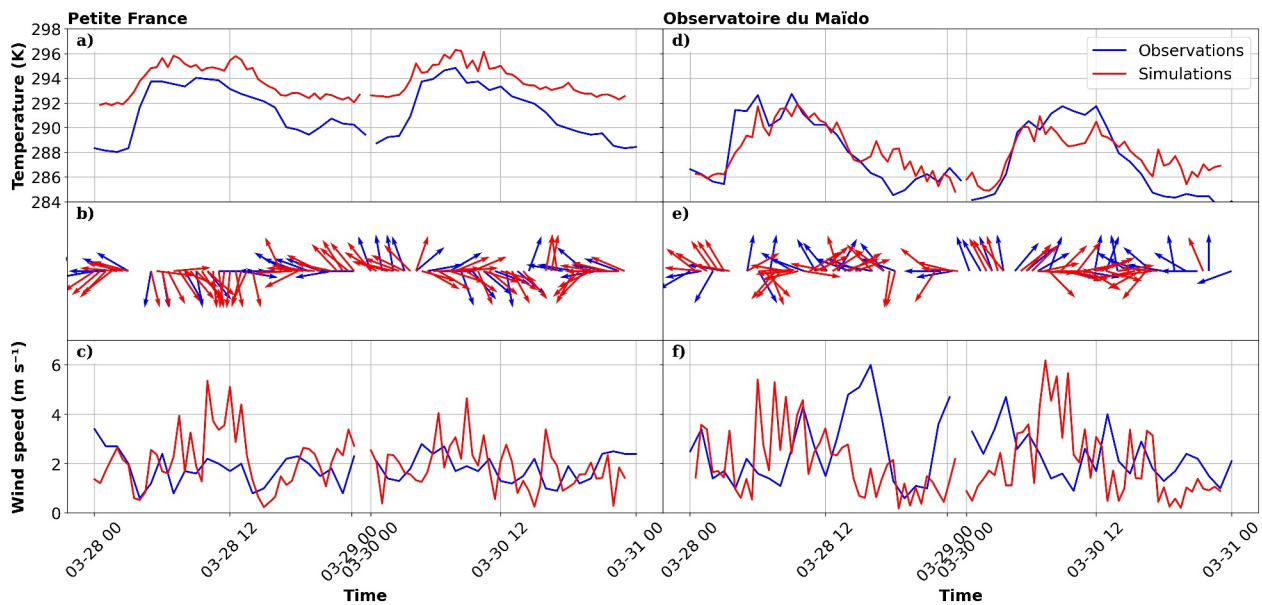

Figure 4. Modeled (red) and observed (blue) time series in PF and MO of (a–d) 2-m temperature, (b–e) 10-m wind direction, and (c–f) 10-m wind speed, on 28 and 30 March.

the west in the afternoon. At night, the wind direction becomes more stable and it blows from the east again. Overall, the wind regime at PF is not influenced by trade winds and so leads to a more stable wind pattern during the day. On the other hand, at MO (Figure 4-e), the wind regime at nighttime (15:00 UTC to 04:00 UTC) is from the east and northeast. At 04:00 UTC, there is a shift in wind direction to the south while during the day there is a variation in wind direction. This is due to the influence of the trade winds on the MO site. At night, the wind direction returns to the east and stays affected by trade winds. These differences in wind direction between the two sites highlight the importance of considering the influence of regional circulation over local meteorological conditions.

In the early morning of 30 March (Figures 4-b and 4-e), the wind direction at both PF and MO stations was from the south–southeast. As the sun rose (02:24 UTC), the wind shifted to the southwest and west direction and by afternoon, between 12:00 UTC and 17:00 UTC at PF, the wind had a slight northwest component. At night, the wind reverted to a descending wind along the slope, blowing from the east at both sites.

The observations from the two stations, PF and MO, suggest that the meteorological conditions on 30 March were different from those observed on 28 March. On the latter day, there was a strong influence from the trade winds. In contrast, on 30 March, the conditions were relatively more stable, with a distinct diurnal cycle of ascending and descending winds that were more noticeable.

Furthermore, the observations from the MO station indicate that the wind is more intense at night, compared to PF, which is likely due to the forcing of the trade winds. Interestingly, the wind weakens to less than 1.5 m s^{-1} during the direction change. During this transition, the wind conditions are favorable for a shift from katabatic to anabatic winds, which is a change from downward flow to upward flow. However, it should be noted that the model overestimates the intensity especially during the day. Certainly, these results suggest that the model is able to reasonably simulate the wind patterns associated with katabatic circulation. The results also highlight the challenges associated with modeling anabatic circulation due to the complexities of boundary layer development and turbulence over slope. Figure B1 in Appendix B presents the modeled and observed time series for the Orchidées and Hotel du Maïdo stations.

3.3. Model Comparison With the Tethered Balloon in DOS

Figure 5 depicts the vertical structure of the atmospheric layer to a height up to 400 m above ground level (a.g.l) at the DOS station for 28 March and 30 March, respectively. The profiles of potential temperature, wind direction, and wind speed are represented for each day. The analysis starts with the flight on 28 March, where the first balloon ascent occurs 1 hr after sunrise, and the last ascent occurs 1 hr after sunset.

The first balloon ascension (Figures 5-a, 5-b, and 5-c) shows an unstable surface layer, a neutral layer between 50 and 170 m, and a stable layer between 170 and 200 m. At 170 m, the winds are more varied and come from the north and northwest at a lesser speed. Throughout the profile, the wind speed stays constant at about 1 m s^{-1}. During the descent of the third flight (Figures 5-d, 5-e, and 5-f), a stable layer is still present, but this time it is stable throughout the vertical profile. The flight lasted almost 3 hr, allowing the atmospheric layer to evolve from a state of instability to stability. The simulation show that the model is able to reproduce the first profile's surface observations, with an unstable layer of warm air near the surface. However, the model fails to simulate the cooling trend observed during the balloon descent (Not showen). Instead, the model's simulation remain around 305.5 K with a bias of 1.5 K. Despite this discrepancy, the model is able to reproduce the stability observed in the vertical profile and the neutral layer between 50 and 170 m. The model accurately simulates the wind direction up to 200 m in the first profile but deviates from the observed direction for the rest of the profile.

The flights of 30 March are illustrated in Figure 5, with the first flight taking place one and a half hours after sunrise and the last flight taking place 1 hr before sunset. In the second flight of 30 March (Figures 5-a', 5-b', and 5-c'), a neutral layer is observed up to 90 m, followed by a stable layer up to 380 m. The model aligns with the observed data during the flight. The descent of the 3rd flight (Figures 5-d', 5-e', and 5-f') shows stability between 100 and 600 m, with anabatic winds at the surface changing to south and southeast at higher altitudes. Surface warming and wind patterns are accurately simulated by the model. Overall, the model correctly simulates anabatic winds on 30 March but struggles to simulate northerly winds on 28 March.

To summarize, the anabatic winds of 30 March are correctly reproduced by the model. On 28 March, the weather conditions are characterized by more intense northerly winds, which the model is unable to simulate correctly. However, the first 200 m characterizing the thermal circulations on slopes are sufficiently well represented by the

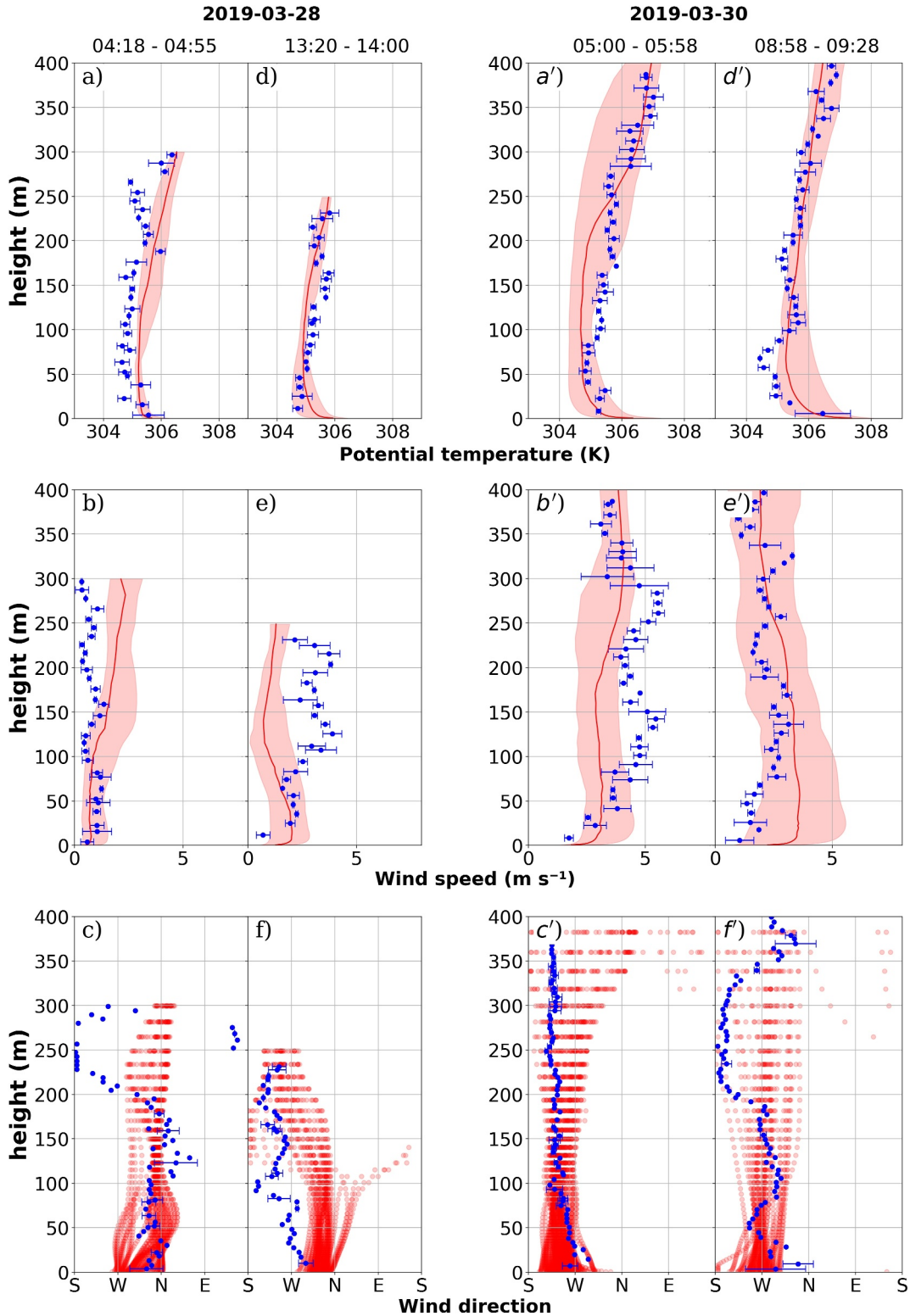

Figure 5. The following figures represent the vertical profiles of a selected flight: (a, a', d, d') potential temperature (K), (b, b', e, e') wind speed (m s^{-1}), and (c, c', f, f') wind direction. The blue dots represent balloon measurements. For potential temperature and wind speed, the shaded red area denotes all profiles simulated during the flight, and the median is indicated by the solid line. For the wind direction, all the simulated profiles are plotted.

model on both days. Given these comparisons, the simulation results can be used to investigate the thermal breeze circulations around Maïdo.

4. Interaction Between Regional Atmospheric Circulations and Local Thermal Circulations

4.1. Dynamic Circulations Over Reunion Island

MesoNH simulation is used to investigate the dynamic circulations over Reunion Island on 28 and 30 March. The analysis focuses on three specific time intervals: 02:00 UTC, 08:00 UTC, and 12:00 UTC, which correspond to 06:00 LT (dawn), 12:00 LT (noon), and 16:00 LT (afternoon), respectively.

The simulation reveal that on 28 March at 02:00 UTC, the island is affected by strong southeast and south trade winds up to 11 m s^{-1}. A trade winds return branch is modeled at the north of the island over the ocean (Figure 6-a). The main part of the island experiences subsiding winds on slopes. The Maïdo region is dominated by southeast winds, which are typical of katabatic slope breezes observed at night. On 30 March (Figure 6-b), weaker trade winds (∼5 m s^{-1}) were simulated, which were not strong enough to form a return circulation near the island. The Maido region was affected by katabatic winds, which are downslope flows.

At 08:00 UTC on 28 March (Figure 6-c), the trade winds became stronger compared to 02 UTC. The branch of the northwesterly leeward circulation is forced in the northwest of the island, and a zone of confluence is modeled at the north of the island. The simulation also reveals a strong penetration of marine air to the north of the island due to the establishment of sea breeze, which also acts as a forcing element for the anabatic slope winds observed along the slopes. The wind regime takes a southwest-to-west component in the western part of the island. This return circulation and the thermal breezes, countering the trade winds, create a convergence zone in the region of the countryside near the Maïdo Observatory. The decrease in trade winds intensity between 28 and 30 March (Figure 6-d) results in the entire island being affected by thermal breezes.

At 12:00 UTC on 28 March (Figure 6-e), the trade winds intensified up to 14 m s^{-1}. The northwesterly leeward return circulation area persists along the slope of the Maïdo. In contrast, on 30 March (Figure 6-f), weaker east trade winds (less than 6.5 m s^{-1}) were simulated. Figure C1 in Appendix C presents the horizontal cross-section of the cloud water column.

4.2. Thermodynamic Circulations Along the Maïdo Slope

Figure 7 shows vertical cross-sections between 0 and 3.5 km over the Maïdo slope along the red line in Figure 6. This is a projection along the axis of the vertical cross-section.

At 02:00 UTC on the 28th (Figure 7-a), katabatic winds are simulated near the surface on the entire slope and have an intensity of 2.1 m s^{-1}. The vertical extension of the flow is limited to ∼30 m a.g.l. Above this layer, a northwestward flow was simulated between 1 and 2 km with wind speeds of 3 m s^{-1}, which corresponds to the return branch circulation of the trade winds. The trade winds were found to exist above 2.5 km with wind speeds reaching up to 6.5 m s^{-1}. In the region between these two layers, a significant TKE of 0.7 m^2 s^{-2} is modeled at around 3 km due to wind shear. On 30 March (Figure 7-b), katabatic winds were simulated also near the surface on the entire slope, but with lower intensity of 1.5 m s^{-1}. As seen before on Figure 6, a significant decrease in the intensity of trade winds is modeled above 1.5 km (∼2.15 m s^{-1}).

At 08:00 UTC on the 28th (Figure 7-c), the vertical cross-section shows the upward northwest flux on the slopes associated with the thermal breeze, reaching a height of 500 m a.g.l with an intensity of 4.4 m s^{-1}. These circulations ascend along the slope up to 2 km, where the descent of trade winds is simulated. At this time, MO is affected by the trade winds, which are considerably strong at high altitudes, reaching a speed of 7.3 m s^{-1}. The formation of cloud droplets is accompanied by the creation of a significant TKE of 1.8 m^2 s^{-2}, resulting from the release of latent heat, which strengthens vertical mixing. The clouds touch the surface at DOS. Besides, on 30 March (Figure 7-d), the trade winds are less intense with wind speeds up to 2.2 m s^{-1}. The anabatic circulation is simulated within a layer that is up to 500 m thick along the entire slope. Furthermore, there is not much cloud cover simulated along the cross-section axis, but rather a spatial extension over the mountains, as shown in Figure 6.

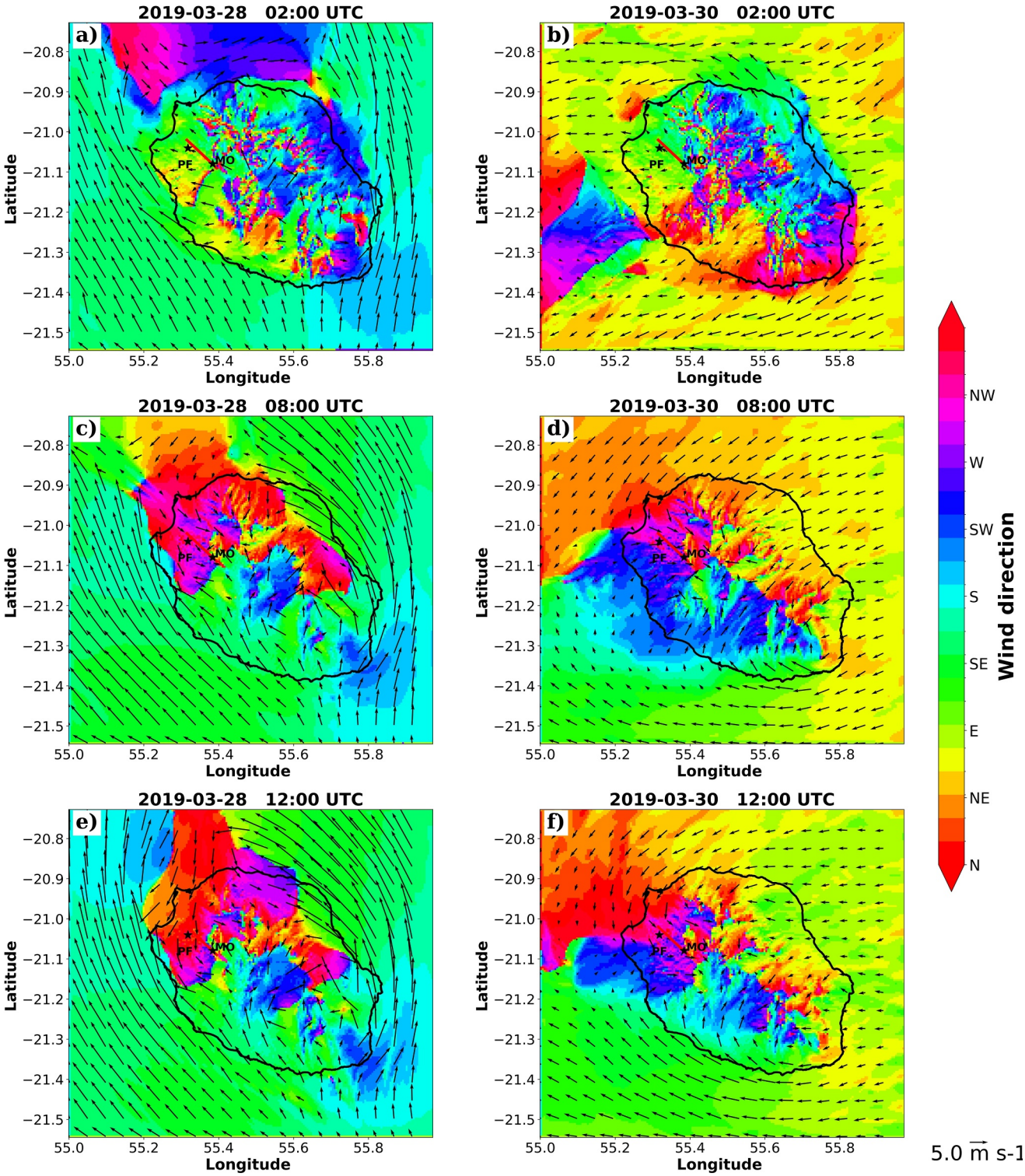

Figure 6. MesoNH simulation: Horizontal cross-section in surface wind direction (color scale) and intensity (arrows in m s^{-1}) at 02:00 UTC (a), 08:00 UTC (c), and 12:00 UTC (e) for 28 March. Similar (b) at 02:00 UTC, (d) 08:00 UTC (f), and at 12:00 UTC for 31 March. PF and MO indicate the location of Petite France station and the Maïdo Observatory, respectively, and the red line indicates the location of the vertical cross-section presented in Figure 7.

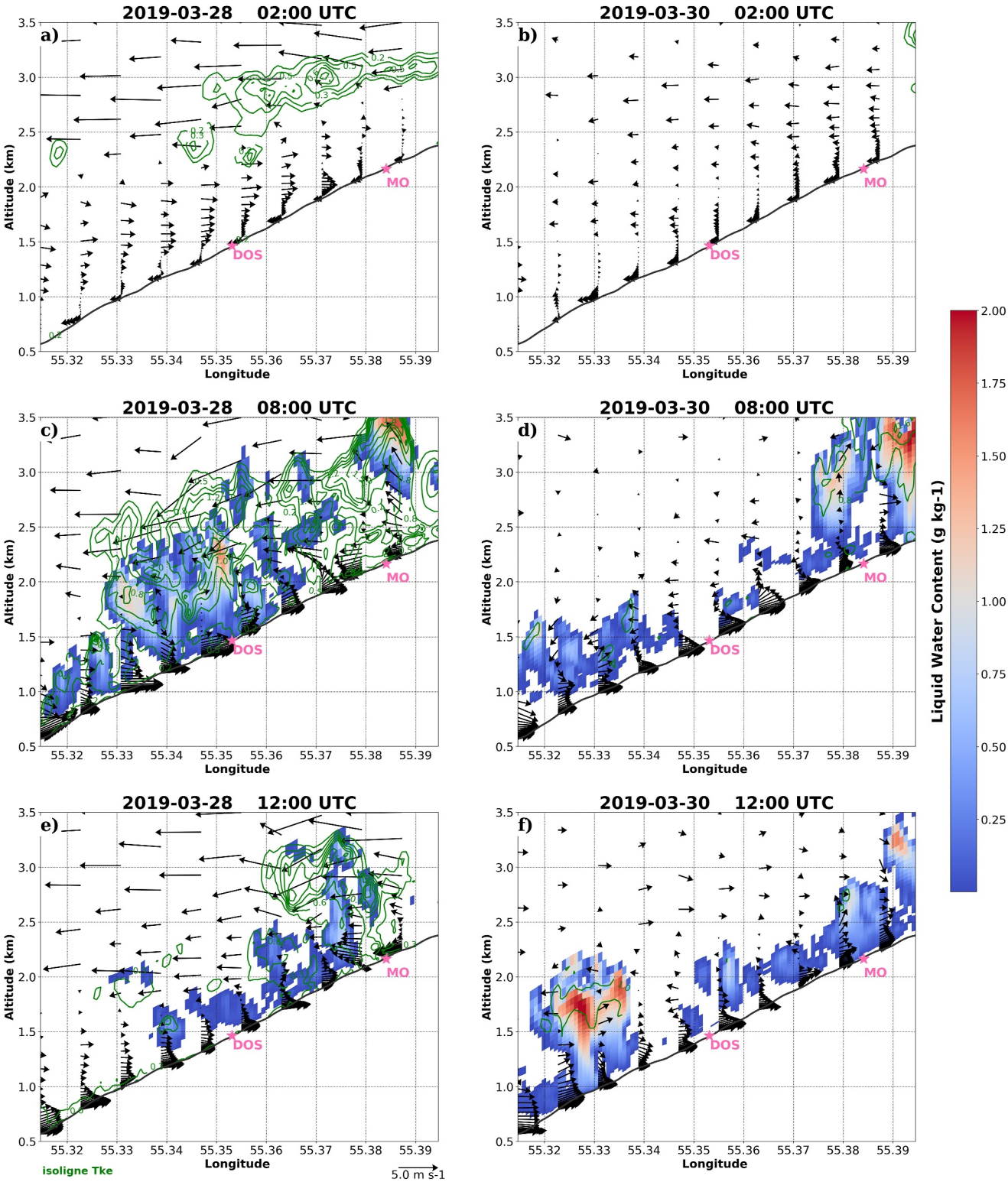

Figure 7. MesoNH simulation: Vertical cross-section shows liquid water content (color scale in g kg^{-1}), wind direction and intensity (vector in m s^{-1}), and Turbulence Kinetic Energy (TKE) (green isoline, in m^2 s^{-2}) at 02:00 UTC (a), 08:00 UTC (c), and 12:00 UTC (e) for 28 March. Similar at 02:00 UTC (b), 08:00 UTC (d), and 12:00 UTC (f) for 30 March.

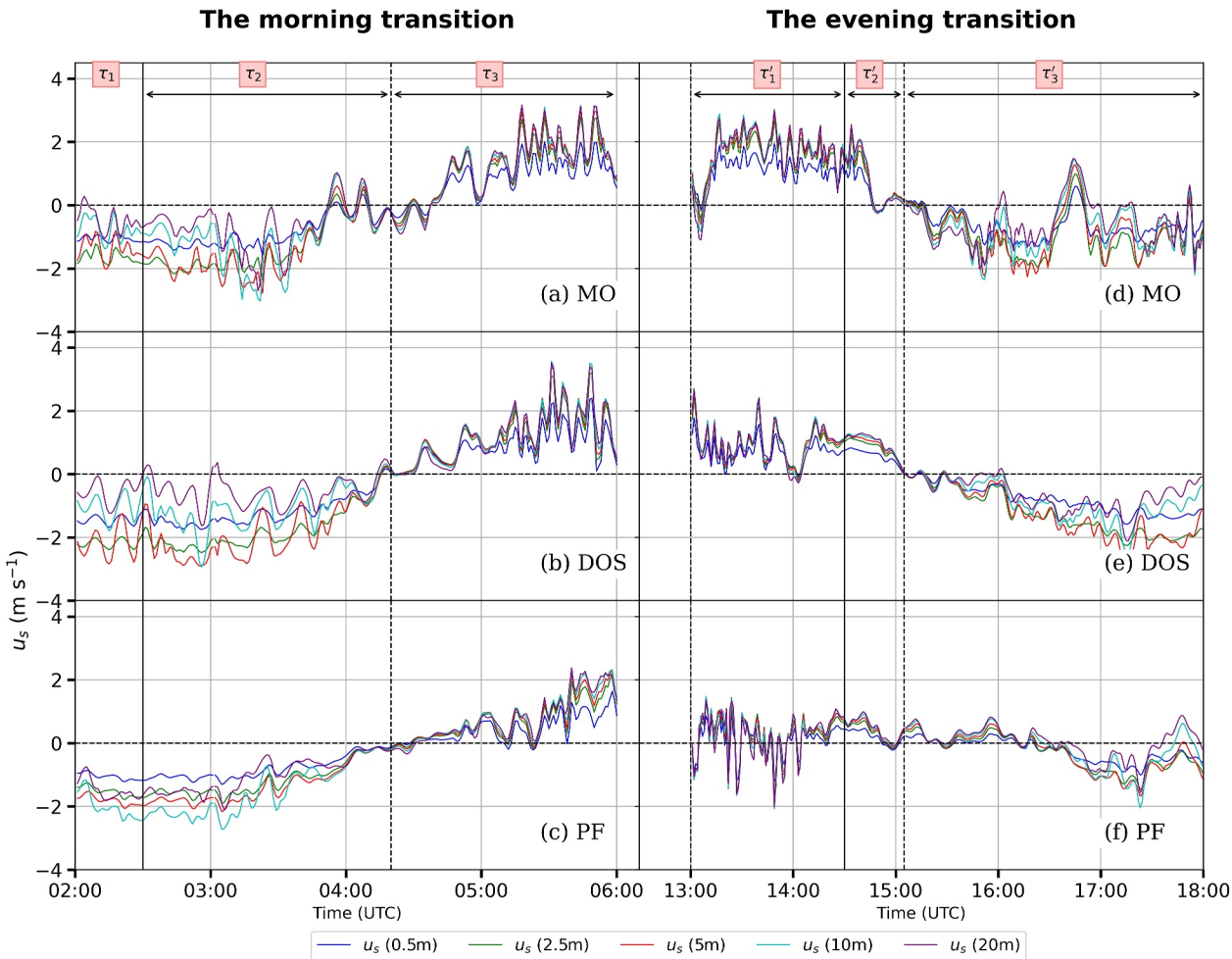

Figure 8. Time series of the along-slope wind velocity during the morning transition and the evening transition at (a and d) MO, (b and e) DOS, and (c and f) PF for 28 March. Negative (positive) velocities indicate upslope (downslope) flow. The black line indicates the sunrise/sunset, and the dotted line indicates the anabatic/katabatic onset.

At 12:00 UTC on the 28th (Figure 7e), the circulation patterns remain the same as at 08:00 UTC, but the trade winds are less intense (6 m s^{-1}). MO is still affected by the trade winds. As noted in Figure 6, the simulation shows the cloud dissipation. However, on the 30th (Figure 7f), clouds are more developed on the slope and the liquid water content reaches 2 g kg^{-1} at 1,700 m a.s.l. over the PF area.

The analysis of these vertical cross-sections shows a complex and highly heterogeneous boundary layer, with several overlapping layers resulting from trade winds, the return branch of the trade winds, and thermal breezes.

5. Momentum and Heat Budget Analysis

In this section, a more in-depth analysis of the results derived from our examination of thermal circulations and their interaction with regional air currents will be conducted. To gain a comprehensive understanding of the mechanisms involved, the model budgets will be inspected with a specific focus on the two periods: the "morning transition" and the "evening transition." The objective is to determine the weight of each term of Equations 1 and 2 in the thermal breeze transition process.

For simplicity's sake, and given the similarity of the processes involved in setting up thermal breezes between 28 March and 30 March, this analysis will be limited to the day of 28 March.

In Figure 8, the ensemble-averaged, along-slope wind velocity time series for selected heights at MO, DOS, and PF are presented. The onset of the anabatic flow occurs approximately 110 min after sunrise. Importantly, the

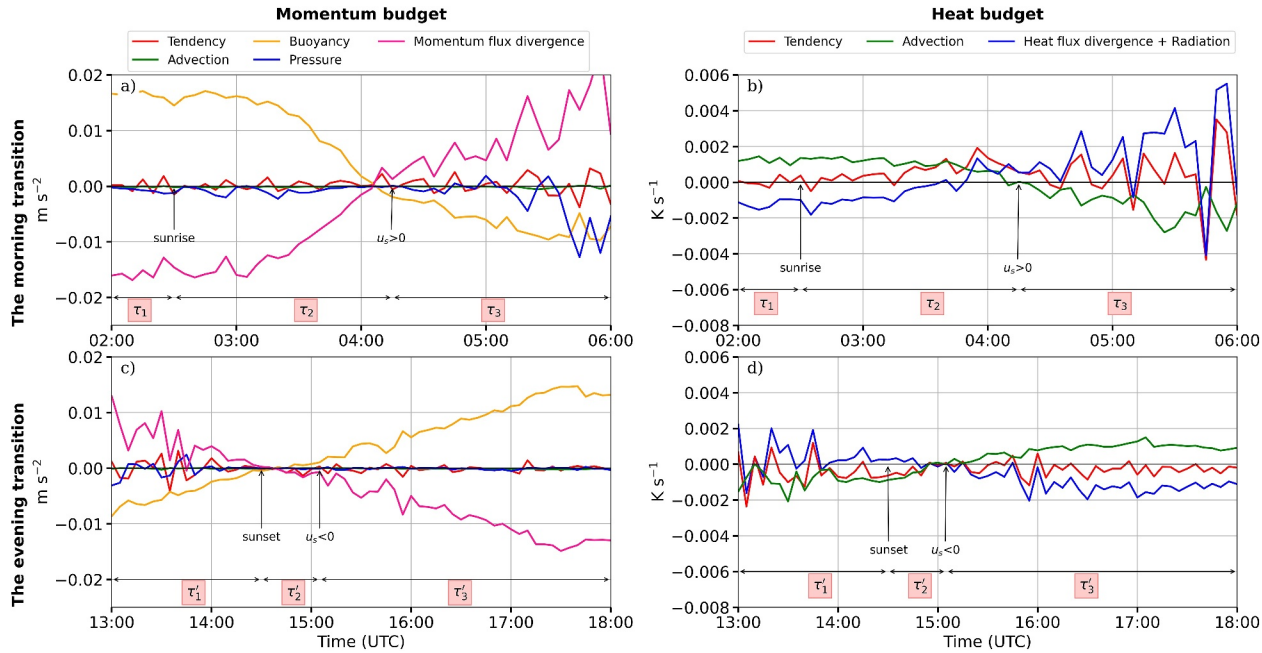

Figure 9. Time series of the surface (5 m) momentum budget and the heat budget in DOS station for the morning and the evening transition; 28 March.

anabatic flow onset is observed within a 20 min interval between PF and MO. Furthermore, it is noted that the anabatic flow initiates very close to the surface and undergoes a gradual deepening process.

As for the katabatic flow, its onset is observed approximately 35 min after sunset, displaying an initiation rate that is three times faster than that of the anabatic flow. Figure 8 also reveals that the highest katabatic velocity is simulated at the heights of 2.5 and 5 m a.g.l., while the lowest is simulated at the 20 m height, exhibiting a variability of 2 m s^{-1}. Conversely, for the anabatic velocity, the variability is less pronounced, being associated with turbulence and a thorough mixing of layers throughout the day. However, it gradually deepens over height at all the stations as observed in the analysis from Jensen et al. (2017).

Having found that the maximum along-slope wind velocity is consistently located around 5 m above ground level in all stations (Figure 8), the evolution of momentum and virtual potential temperature budgets along the slopes of Maïdo at this height will now be examined. The temporal evolution of momentum and heat budget terms in DOS is examined for both the morning (Figures 9a and 9b) and evening transition (Figures 9-c and 9-d), as illustrated in Figure 9.

At 02:23 UTC (Figure 9b), the sun rises. By 03:50 UTC, radiation warms the surface with a delay due to the northwest-facing slope. This orientation delays the sunlight's impact, affecting the timing of warming, which then heats up the layer above through heat flux divergence. As a result, a buoyancy acceleration in momentum budget (Figure 9a) becomes the dominant source of momentum influenced by local surface heating and is essentially compensated by momentum flux divergence. The anabatic flow onset starts 10 min after the shift of buoyancy acceleration. After the anabatic flow is established, heat advection, which exhibits a nearly symmetrical evolution compared to heat flux divergence, commences simultaneously.

During the evening transition, prior to the initiation of the katabatic flow (depicted in Figures 9-c and 9-d), the cooling of the lower surface layer occurs primarily due to kinematic heat flux divergence and radiation, thereby providing optimal conditions for the transition, as observed in Jensen et al. (2017) analysis. At the same time, the turbulent flux divergence creates momentum, indicating the emergence of convection just below the lowest level before the observed onset. Once the katabatic flow is established, buoyancy acceleration becomes the dominant source again of momentum, now influenced by local surface cooling and also compensated by momentum flux divergence.

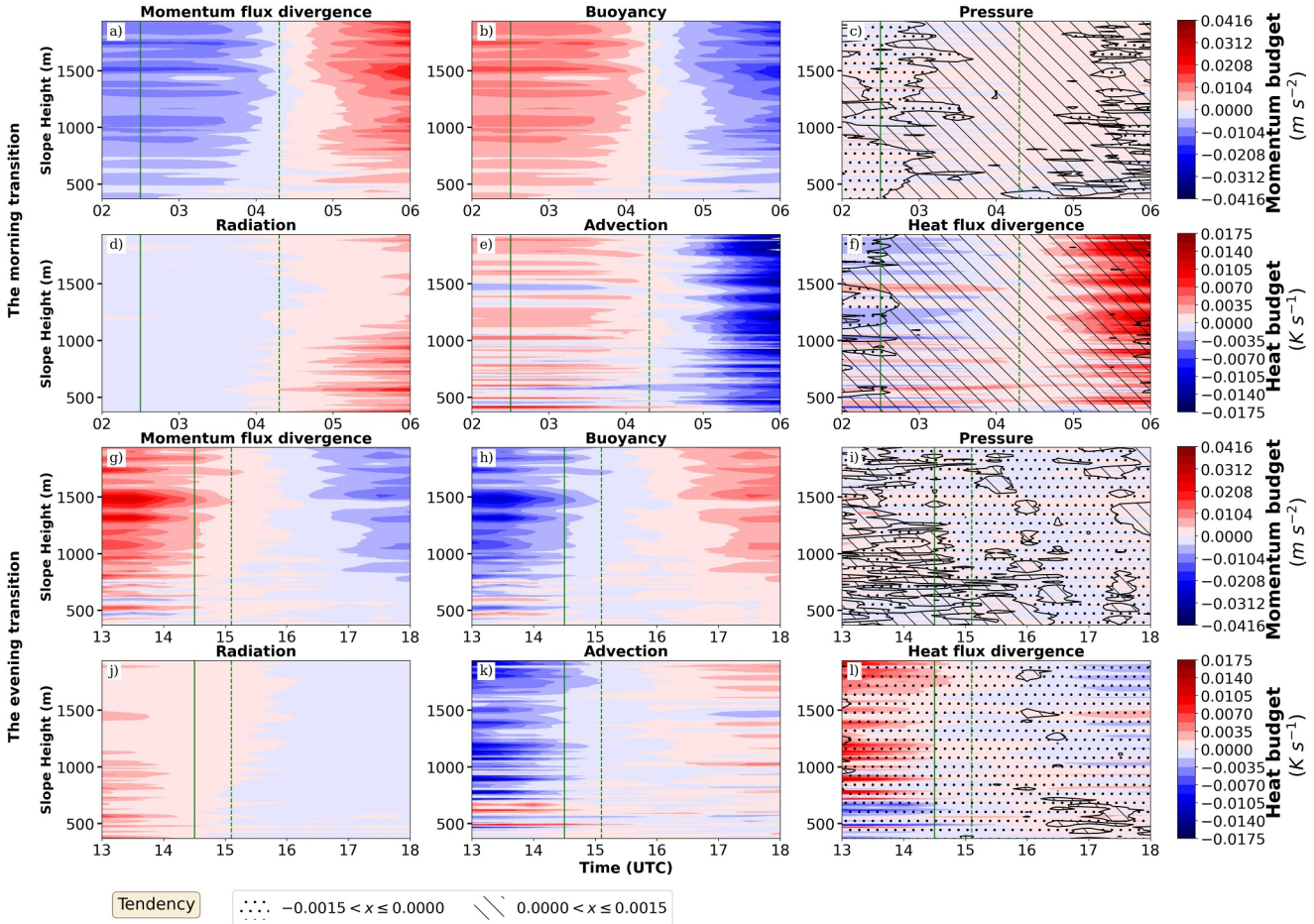

Figure 10. Valley cross sections of the momentum budget terms: (a and g) momentum flux divergence, (b and h) buoyancy acceleration, and (c and i) pressure gradient, and of the heat budget terms: (d and j) radiation, (e and k) advection, (f and l) heat flux divergence, and the tendency of momentum and heat (isoline) during the morning transition and the evening transition for 28 March. The green line indicates the sunrise/sunset, and the dotted line indicates the anabatic/katabatic onset.

The results are in line with the findings of Arrillaga et al. (2019) for weak downslope situations where wind speeds during the evening transition are lower than 1.5 m s^{-1}. The study highlights that katabatic flows, primarily driven by buoyancy, occur when large-scale winds oppose downslope flow and soil moisture is higher than the summer median. These flows are characterized by very low intensity and are situated below 3 m s^{-1}.

Drawing from the study by Nadeau et al. (2013), which featured a slope similar to that of Maïdo (in the Swiss Alps), it was revealed that after sunset, the katabatic flow experiences a reversal. This phenomenon is well described by a proposed time scale that balances inertial and buoyancy forces. Notably, it typically takes approximately 1.5 hr for the katabatic flow to reach a quasi-equilibrium state during this period, which is almost the same time frame as the establishment of our katabatic circulation. Additionally, Nadeau et al. (2013) emphasized the significant role of radiative flux divergence in the early nighttime phase.

To deepen our understanding of these terms, Figure 10 is turned to, wherein valley cross-sections illustrate various components of the momentum and heat budgets. A spatial perspective is provided, revealing how these processes evolve along the slope.

In Figure 10, during the morning transition, the summit of the slope reveals the peak values for both the momentum flux divergence (Figure 10-a) and buoyancy acceleration (Figure 10-b) terms (0.043 m s^{-2}), coinciding with the region of highest temperature gradient (not shown). The spatial evolution of these two terms occurs over several minutes across the Maïdo slope and becomes more homogeneous across the slope after the onset of the anabatic flow. With positive gradient of pressure (Figure 10-c) indicating the onset of the anabatic flow and a change in tendency of momentum that also becomes positive. The radiation term (Figure 10-d) clearly demonstrates surface

warming occurring at 500 m, gradually deepening over the height of the slope. Additionally, warming is observed above 1,600 m directly linked to the slope's exposure. This triggers cold air advection along the slope after the onset of the anabatic flow which, in turn, is compensated by positive heat flux divergence (Figure 10-f). Furthermore, the heat tendency also changes sign during the transition period and exhibits a maximum of 0.0016 K s^{-1} above 1,200 m a.s.l. When the anabatic flow is established.

Similar to the morning transition, the momentum flux divergence (Figure 10-g) and buoyancy (Figure 10-h) during the evening transition change sign at the base of the slope but this time it takes less time for their spatial evolution to reach the summit of the slope while remaining stronger at the summit. The pressure gradient (Figure 10-i) is moderately negative with a global change in tendency that also becomes negative. The surface cooling starts at the base of the slope as seen in the radiation term (Figure 10-j) and sets off warm advection along the slope (Figure 10-k). This is compensated by a negative heat flux divergence (Figure 10-l) and so indicates a mix of cold air through turbulence. During this transition, the heat tendency (Figure 10-l) exhibits primarily negative values with −0.0016 K s^{-1} being the maximum simulated during the establishment of the katabatic flow.

6. Summary and Conclusion

The aim of this study is to investigate the mechanisms behind thermal circulations on slopes, with a focus on Reunion Island. Observations collected during the BIO-MAÏDO campaign from 11 March to 7 April 2019 as well as high-resolution simulation generated by the MesoNH model with a horizontal resolution of 100 m and a vertical resolution of approximately 1 m near the surface were analyzed to achieve this work.

The analysis of wind regimes at the mid-slope and mountain summit revealed two distinct periods. During the nighttime, easterly and southeasterly winds dominated at 10 m while during the daytime, west and northwesterly winds prevailed. This pattern corresponds to the presence of katabatic/anabatic flows and trade winds at the summit and katabatic/anabatic flows at the mid-slope. The temporal evolution of 2-m temperature and 10-m wind speed and direction at PF and MO stations on 28 March and 30 March highlighted differences in temperature and wind patterns between the two sites with temperature differences ranging from 2° to 4° Celsius throughout the day. Furthermore, the measurements were used to validate the model which enabled the investigation of thermal breeze circulations.

Katabatic and anabatic winds during dawn and noon are strongly influenced by the intensity of the trade winds. On 28 March, the intense trade winds allowed for the development of the return circulation of the trade winds at the northwest of the island, while on 30 March, the development of this circulation was prevented by less intense trade winds (∼5 m s^{-1}). Furthermore, the strengthening of trade winds at noon and during the afternoon on the 28th created a pronounced return branch circulation of the trade winds that rose along the slope, which was not present on 30 March. The simulation also show multiple layered structures: katabatic winds near the surface, with varying intensities, as well as northwestward flow representing the return branch circulation of the trade winds, and trade winds at higher altitudes above 2 km. The presence of clouds and kinetic turbulence adds complexity to the boundary layer.

The analysis of the breeze establishment period was conducted based on the along-slope wind velocity. The findings reveal that the katabatic flow reaches a quasi-equilibrium approximately 35 min after the local sunset which is three times faster than the anabatic flow. The highest katabatic velocities are simulated at heights of 2.5 and 5 m while the lowest velocities occur at 20 m, exhibiting a variability of 2 m s^{-1}.

The investigation of momentum and virtual potential temperature budgets along Maïdo's slopes at 5 m height reveals peak values for pressure and buoyancy terms at the summit, aligning with the region of the highest temperature gradient. Notably, surface warming triggers cold advection after the anabatic flow onset, while surface cooling induces warm advection during the morning transition.

Further examination of momentum and heat budget terms in DOS during morning and evening transitions exposes distinct temporal variations, indicating different phases of the thermal circulation. Surface heating and cooling influence buoyancy acceleration as the dominant momentum source during the anabatic and katabatic flow onsets, respectively, compensated by momentum flux divergence. Buoyancy acceleration, influenced by local surface heating for the anabatic flow onset, and local surface cooling for the katabatic flow onset, emerge as

the primary drivers of the thermal circulations as simulated in the temporal evolution of momentum and heat budget terms in DOS.

The results presented here demonstrate an adequate methodology for studying thermal circulations. As highlighted in the literature, the method used in this study can be effectively applied to different types of breezes and is applicable to complex terrains. Beyond this, these insights can potentially extend to comparative analyses with other studies, particularly as islands experience strong thermal forcing. This generalizability is especially relevant for tropical islands, which are also influenced by other types of circulations such as the trade winds. As presented, these winds play a significant role, particularly in creating convergence zones.

In conclusion, the essential role of high-resolution modeling in understanding and integrating the complex processes that occur in complex terrain like Reunion Island has been demonstrated in this study. Although this analysis focused on two cases, complementing it with climatology studies could allow further exploration of the variations of thermal circulations over different wind regimes, such as the intense trade winds from June to August, compared to the weak and moderate trade winds from December to February.

Appendix A: Comparison of Observed and Modeled Data—Calculation Methods and Results for Bias and Root Mean Square Error (RMSE)

A comparative analysis of meteorological simulations was conducted using data from 16 stations, categorized by altitude: Group 1 [6 stations] (<100 m), Group 2 [3 stations] (100 m < alt <500 m), Group 3 [4 stations] (500 m < alt <1,500°m), and Group 4 [3 stations] (>1,500 m). The hourly data from meteorological stations were used for observations, and simulation parameters (air temperature, wind speed, wind direction, and humidity) were averaged over 1 hr to ensure a fair comparison. For temperature, Group 1 exhibited a median bias of approximately −0.5°C, indicating a slight underestimation of observed temperatures. Groups 2, 3, and 4 showed median biases of 0.1°, 0°, and −0.5°C, respectively, with Group 2 slightly overestimating and Groups 1 and 4 underestimating temperatures. The median RMSE values were 2°, 1.5°, 1.25°, and 1.75°C for Groups 1, 2, 3, and 4, suggesting more realistic simulations for Group 3 and Group 2. Wind speed simulations showed a median bias of 1.3 m s^{-1} for Group 1, indicating an overestimation of wind speeds. Groups 2, 3, and 4 exhibited biases of 0.4, 0.5, and 1.2 m s^{-1}, respectively, with Group 1 and Group 4 overestimating wind speeds more significantly. The RMSE values were 2.3, 0.75, 1.2, and 2 m s^{-1}, indicating better accuracy for Group 3. Relative humidity simulations displayed median biases of 2.5% for Group 1%, −2.5% for Group 2%, −2.5% for Group 3%, and −7% for Group 4. Group one overestimated humidity, while Groups 2, 3, and 4 underestimated it, with Group 4 having the largest underestimation. The RMSE values were 8%, 6%, 13%, and 12%, suggesting that the simulations are more accurate for Group 2 and Group 3 and less so for Groups 1 and 4. These results demonstrate that the simulations are generally more accurate for temperature and wind speed in Group 3 and for relative humidity in Groups 2 and 3. For wind direction, Group 1 exhibited a median bias of approximately 13°, indicating a slight difference compared to the observed wind direction. This suggests that the model's wind direction predictions are relatively accurate for this group. Groups 2, 3, and 4 showed median biases of 1°, −14°, and −20°, respectively. Group 2's bias of 1° implies an excellent agreement between the model and observations, indicating that the model captures the wind direction very well. Group 3's bias of −14° still represents a reasonably accurate prediction, as deviations of this magnitude are typically within acceptable limits for meteorological modeling. However, for Group 4, the bias of −20° suggests more substantial discrepancies between the model and observed data. The median RMSE values were 71°, 82°, 74°, and 86° for Groups 1, 2, 3, and 4, respectively. These RMSE values indicate that Group 1 had the most realistic simulations overall, while Groups 2 and 3 also performed reasonably well. Group 4's higher RMSE reflects the increased difficulty in accurately simulating wind directions for these stations. For Group 4, the simulated wind directions show significant discrepancies compared to the observed data. This difficulty can be attributed to the fact that stations in Group 4 are often located near summits, such as the Maïdo Observatory, which are in convergence zones significantly affected by both general circulations (trade winds) and local circulations. These areas are also sensitive to convective zones (downdrafts, rain), which are challenging to accurately represent in simulations. Therefore, the larger bias and higher RMSE for Group 4 are expected and highlight the complexities involved in modeling wind directions in such dynamic and topographically complex regions. (Figures A1 and A2).

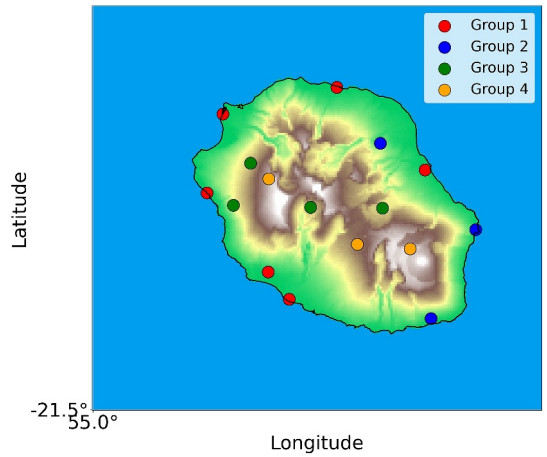

Figure A1. Locations of meteorological stations on the island, categorized by altitude and represented by different colors: Group 1 (red) includes 6 stations located at elevations below 100 m, Group 2 (blue) includes 3 stations located at elevations between 100 and 500 m, Group 3 (green) includes 4 stations located at elevations between 500 and 1,500 m, and Group 4 (orange) includes 3 stations located at elevations above 1,500 m.

A1. Calculation of Bias and Root Mean Square Error (RMSE)

1. Bias is a measure of the average difference between observed values and modeled values. It indicates whether, on average, the model underestimates or overestimates the observations. Bias is calculated using the following formula:

$$\text{Bias} = \frac{1}{N}\sum_{i=1}^{N}(\text{ModeledValue}_i - \text{ObservedValue}_i) \tag{A1}$$

For angular variables such as wind direction, the difference between angles must be calculated carefully to account for the circular nature of angles. The difference is calculated using the formula:

$$\text{AngleDifference} = (\text{modeled} - \text{observed} + 180) \bmod 360 - 180 \tag{A2}$$

where: modeled is the modeled wind direction in degrees and observed is the observed wind direction in degrees.
The Bias for wind direction is calculated using circular statistics. The circular mean accounts for the periodicity of angles. The formula for the circular bias is:

a. Convert angle differences to radians:

$$\text{AngleDifferenceInRadians} = \frac{\pi}{180} \times \text{AngleDifference} \tag{A3}$$

b. Calculate the mean sine and cosine of the differences:

$$\text{MeanSine} = \frac{1}{N}\sum_{i=1}^{N}\sin\left(\text{AngleDifferenceInRadians}_i\right) \tag{A4}$$

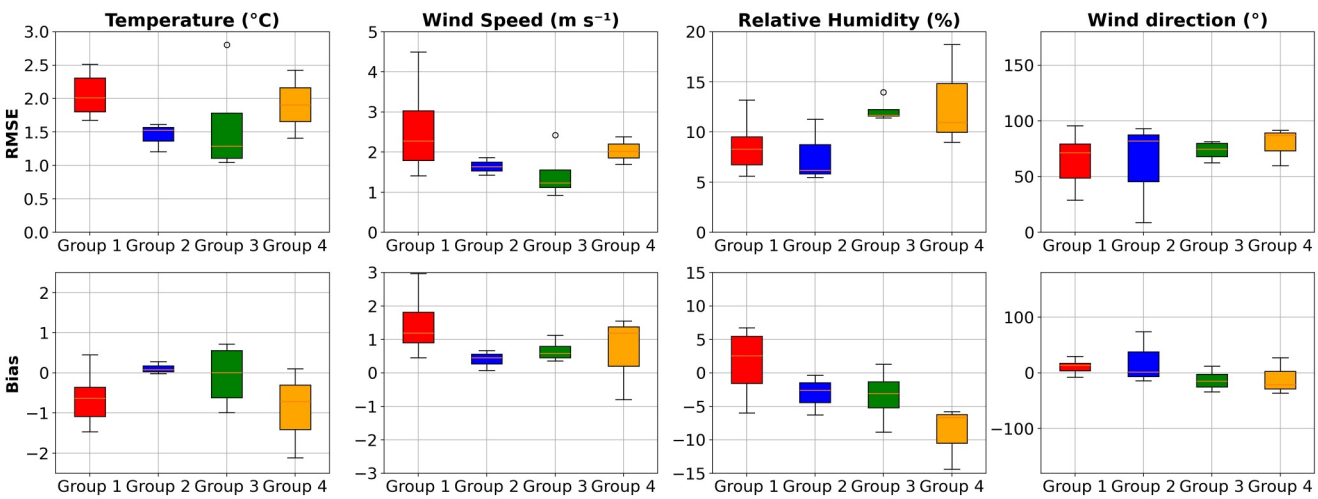

Figure A2. Box plots comparing the Root Mean Square Error (RMSE) and Bias for different meteorological variables across four groups of stations for 28 March, 2019. The meteorological variables analyzed are (a) Temperature (°C), (b) Wind Speed (m s^{-1}), (c) Relative Humidity (%), and (d) Wind Direction (°). The upper row of plots shows the RMSE, while the lower row shows the Bias. The data was collected from Météo-France stations and compared with simulation results for the specified day. The box plots illustrate the distribution of errors and biases in the simulation compared to observed data, with the central line indicating the median, the box representing the interquartile range, and the whiskers extending to 1.5 times the interquartile range. Outliers are indicated by circles.

$$\text{MeanCosine} = \frac{1}{N}\sum_{i=1}^{N}\cos\left(\text{AngleDifferenceInRadians}_i\right) \tag{A5}$$

c. Compute the circular mean:

$$\text{CircularMean} = \arctan 2(\text{MeanSine}, \text{MeanCosine}) \tag{A6}$$

d. Convert the circular mean back to degrees:

$$\text{Bias} = \frac{180}{\pi} \times \text{CircularMean} \tag{A7}$$

2. The RMSE is a measure of the average quadratic error between observed values and modeled values. It provides an indication of the magnitude of the prediction errors. The RMSE is calculated using the following formula:

$$\text{RMSE} = \sqrt{\frac{1}{N}\sum_{i=1}^{N}(\text{ModeledValue}_i - \text{ObservedValue}_i)^2} \tag{A8}$$

N is the total number of data points. ModeledValue is the modeled value for the i-th data point. ObservedValue is the observed value for the i-th data point.
The RMSE for wind direction is calculated on the angular differences. The formula is:

$$\text{RMSE} = \sqrt{\frac{1}{N}\sum_{i=1}^{N}\left(\text{AngleDifference}_i\right)^2} \tag{A9}$$

where AngleDifference is the angular difference for the data point.

The calculations of bias and RMSE are performed for each group of data corresponding to a specific station. The statistics are calculated on an hourly basis for each station.

Appendix B: Modeled and Observed Time Series: Orchidées and Hotel Du Maïdo

A comparative analysis of MesoNH model simulations and observational data from the Orchidées (DOS) and Hotel du Maido (HM) stations for 28 and 30 March is presented in Figure B1, focusing on 2-m temperature, 10-m wind speed, and wind direction. The model generally captures the diurnal temperature cycle at both stations, with DOS showing a consistent warm bias of 1–2 K, increasing to 3 K during nighttime, while HM exhibits better agreement with deviations typically under 1 K. The timing of temperature maxima and minima is well-represented, indicating accurate simulation of the diurnal cycle. Wind direction transitions coinciding with sunrise and sunset are observed, indicating shifts between katabatic and anabatic winds. The model captures these day/night transitions and overall directional trends, though discrepancies of 45°to 90° are noted during transitional periods. The most significant issue is the model's overestimation of wind speed, particularly at HM. At DOS, wind speeds are generally overestimated by 1–2 (m s^{-1}), while HM shows more pronounced overestimation of 2–4 (m s^{-1}), with peaks reaching 5 (m s^{-1}) above observed values. The model also exaggerates the amplitude of diurnal wind speed variations. Overall, temperature simulations show better accuracy compared to wind parameters. The systematic overestimation of wind speed may point to issues in surface roughness representation or turbulence parameterization in complex terrain, highlighting areas for potential improvement in the model's performance in complex topographical settings.

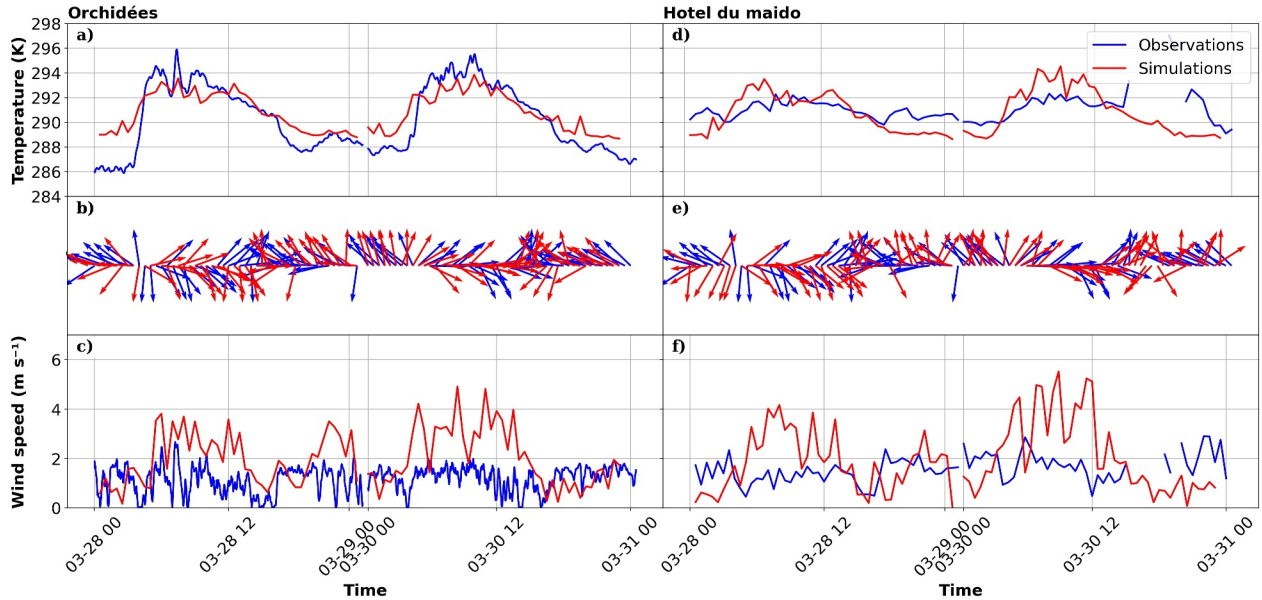

Figure B1. Modeled (red) and observed (blue) time series in DOS and HM of (a–d) 2-m temperature, (b–e) 10-m wind direction, and (c–f) 10-m wind speed, on 28 and 30 March.

Appendix C: Horizontal Cross-Section of Cloud Water Column

(See Figure C1).

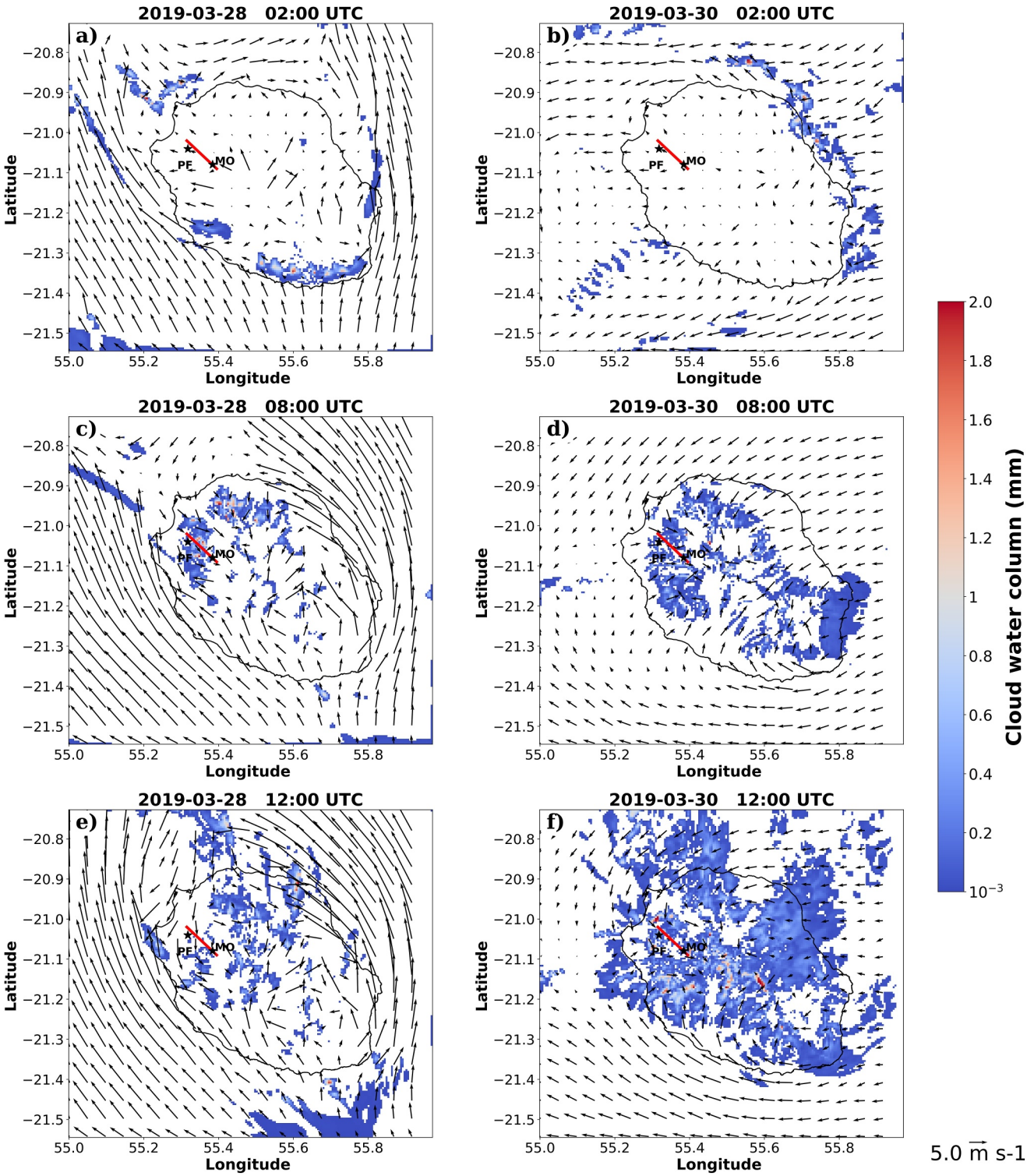

Figure C1. MesoNH simulation: Horizontal cross-section in surface and intensity (arrows in m s^{-1}) and cloud water column (mm) at 02:00 UTC (a), 08:00 UTC (c), and 12:00 UTC (e) for 28 March. Similar (b) at 02:00 UTC, (d) 08:00 UTC (f), and at 12:00 UTC for 31 March. PF and MO indicate the location of Petite France station and the Maïdo Observatory, respectively, and the red line indicates the location of the vertical cross-section presented in Figure 7.

Data Availability Statement

The MesoNH code is open source and can be found at http://mesonh.aero.obs-mip.fr (accessed on 16 November 2023). The version I utilized is 5.5.1, which is downloadable from the website. The code is useable on any platform. As for the BIO-MAÏDO campaign data, it is available on the AERIS open data portal: https://www.aeris-data.fr/catalogue/ (accessed on 16 November 2023). To access the data, an account (free of charge) must be created, and searching for BIO-MAIDO in the catalog will provide access to the data.

Acknowledgments
The authors would like to express their gratitude to F. Gheusi, V. Duflot, J. Cuxart and C. Brun for their valuable contributions to our scientific discussions. We are also appreciative of P. Wautelet and the MesoNH support team for their essential assistance and feedback. Furthermore, our sincere thanks are extended to all BIOMAIDO participants from LACy, OSU-R, CNRM, LaMP, ATMO-Réunion, IGE, LaRGE, LOA, LSCE, and LAERO. Meso-NH simulation have been made on the Météo-France supercomputer. The BIO-MAÏDO project was funded by the Agence Nationale de la Recherche (ANR-18-CE01-0013).

References

Arrillaga, J. A., Yagüe, C., Román-Cascón, C., Sastre, M., Jiménez, M. A., Maqueda, G., & Vilà-Guerau de Arellano, J. (2019). From weak to intense downslope winds: Origin, interaction with boundary-layer turbulence and impact on CO_2 variability. *Atmospheric Chemistry and Physics*, *19*(7), 4615–4635. https://doi.org/10.5194/acp-19-4615-2019

Baray, J.-L., Courcoux, Y., Keckhut, P., Portafaix, T., Tulet, P., Cammas, J.-P., et al. (2013). Maïdo observatory: A new high-altitude station facility at reunion island (21°S, 55°E) for long-term atmospheric remote sensing and in situ measurements. *Atmospheric Measurement Techniques*, *6*(10), 2865–2877. https://doi.org/10.5194/amt-6-2865-2013

Blein, S. (2016). Observation et modélisation de couche limite atmosphérique stable en relief complexe: Le processus turbulent d'écoulement catabatique (phdthesis, Université Grenoble Alpes). Retrieved from https://theses.hal.science/tel-01622676

Bougeault, P., & Lacarrere, P. (1989). Parameterization of orography-induced turbulence in a mesobeta–scale model. *Monthly Weather Review*, *117*(8), 1872–1890. https://doi.org/10.1175/1520-0493(1989)117⟨1872:POOITI⟩2.0.CO;2

Carlis, D. L., Chen, Y.-L., & Morris, V. R. (2010). Numerical simulations of island-scale airflow over Maui and the Maui vortex under summer trade wind conditions. *Monthly Weather Review*, *138*(7), 2706–2736. https://doi.org/10.1175/2009mwr3236.1

Cécé, R., Bernard, D., d'Alexis, C., & Dorville, J.-F. (2014). Numerical simulations of Island-induced circulations and windward katabatic flow over the Guadeloupe Archipelago. *Monthly Weather Review*, *142*(2), 850–867. https://doi.org/10.1175/MWR-D-13-00119.1

Chemel, C., Arduini, G., Staquet, C., Largeron, Y., Legain, D., Tzanos, D., & Paci, A. (2016). Valley heat deficit as a bulk measure of wintertime particulate air pollution in the Arve River Valley. *Atmospheric Environment*, *128*, 208–215. https://doi.org/10.1016/j.atmosenv.2015.12.058

Colella, P., & Woodward, P. R. (1984). The Piecewise Parabolic Method (PPM) for gas-dynamical simulations. *Journal of Computational Physics*, *54*(1), 174–201. https://doi.org/10.1016/0021-9991(84)90143-8

Cuxart, J. (2015). When can a high-resolution simulation over complex terrain be called LES? *Frontiers in Earth Science*, *3*, 87. https://doi.org/10.3389/feart.2015.00087

Cuxart, J., Bougeault, P., & Redelsperger, J.-L. (2000). A turbulence scheme allowing for mesoscale and large-eddy simulations. *Quarterly Journal of the Royal Meteorological Society*, *126*(562), 1–30. https://doi.org/10.1002/qj.49712656202

Cuxart, J., Jiménez, M. A., Telišman Prtenjak, M., & Grisogono, B. (2014). Study of a sea-breeze case through momentum, temperature, and turbulence budgets. *Journal of Applied Meteorology and Climatology*, *53*(11), 2589–2609. https://doi.org/10.1175/JAMC-D-14-0007.1

Deardorff, J. W. (1974). Three-dimensional numerical study of the height and mean structure of a heated planetary boundary layer. *Boundary-Layer Meteorology*, *7*(1), 81–106. https://doi.org/10.1007/BF00224974

Dominutti, P. A., Renard, P., Vaïtilingom, M., Bianco, A., Baray, J.-L., Borbon, A., et al. (2022). Insights into tropical cloud chemistry in Réunion (Indian ocean): Results from the BIO-Maïdo campaign. *Atmospheric Chemistry and Physics*, *22*(1), 505–533. https://doi.org/10.5194/acp-22-505-2022

Duflot, V., Tulet, P., Flores, O., Barthe, C., Colomb, A., Deguillaume, L., et al. (2019). Preliminary results from the FARCE 2015 campaign: Multidisciplinary study of the forest–gas–aerosol–cloud system on the tropical island of La Réunion. *Atmospheric Chemistry and Physics*, *19*(16), 10591–10618. https://doi.org/10.5194/acp-19-10591-2019

Duine, G.-J., Hedde, T., Roubin, P., Durand, P., Lothon, M., Lohou, F., et al. (2017). Characterization of valley flows within two confluent valleys under stable conditions: Observations from the KASCADE field experiment. *Quarterly Journal of the Royal Meteorological Society*, *143*(705), 1886–1902. https://doi.org/10.1002/qj.3049

Durand, J., Tulet, P., Leriche, M., Bielli, S., Villeneuve, N., Muro, A. D., & Fillipi, J.-B. (2014). Modeling the lava heat flux during severe effusive volcanic eruption: An important impact on surface air quality. *Journal of Geophysical Research: Atmospheres*, *119*(20), 11729–17421. https://doi.org/10.1002/2014JD022034

Foucart, B., Sellegri, K., Tulet, P., Rose, C., Metzger, J.-M., & Picard, D. (2018). High occurrence of new particle formation events at the Maïdo high-altitude observatory (2150 m), Réunion (Indian Ocean). *Atmospheric Chemistry and Physics*, *18*(13), 9243–9261. https://doi.org/10.5194/acp-18-9243-2018

Gal-Chen, T., & Somerville, R. C. J. (1975). On the use of a coordinate transformation for the solution of the Navier-Stokes equations. *Journal of Computational Physics*, *17*(2), 209–228. https://doi.org/10.1016/0021-9991(75)90037-6

Giovannini, L., Laiti, L., Serafin, S., & Zardi, D. (2017). The thermally driven diurnal wind system of the Adige Valley in the Italian Alps. *Quarterly Journal of the Royal Meteorological Society*, *143*(707), 2389–2402. https://doi.org/10.1002/qj.3092

Jensen, D. D., Nadeau, D. F., Hoch, S. W., & Pardyjak, E. R. (2017). The evolution and sensitivity of katabatic flow dynamics to external influences through the evening transition. *Quarterly Journal of the Royal Meteorological Society*, *143*(702), 423–438. https://doi.org/10.1002/qj.2932

Jiang, G.-S., & Shu, C.-W. (1996). Efficient implementation of weighted ENO schemes. *Journal of Computational Physics*, *126*(1), 202–228. https://doi.org/10.1006/jcph.1996.0130

Lac, C., Chaboureau, J.-P., Masson, V., Pinty, J.-P., Tulet, P., Escobar, J., et al. (2018). Overview of the Meso-NH model version 5.4 and its applications. *Geoscientific Model Development*, *11*(5), 1929–1969. https://doi.org/10.5194/gmd-11-1929-2018

Lafore, J. P., Stein, J., Asencio, N., Bougeault, P., Ducrocq, V., Duron, J., et al. (1998). The Meso-NH atmospheric simulation system. Part I: Adiabatic formulation and control simulations. *Annales Geophysicae*, *16*(1), 90–109. https://doi.org/10.1007/s00585-997-0090-6

Leriche, M., Tulet, P., Deguillaume, L., Burnet, F., Colomb, A., Jambert, C., et al. (2023). Measurement report: Bio-physicochemistry of tropical clouds at ma Ido (R'eunion island, Indian ocean): Overview of results from the BIO-MAÏDO campaign. *EGUsphere*, 1–45. https://doi.org/10.5194/egusphere-2023-1362

Lesouëf, D. (2010). Étude numérique des circulations locales à la Réunion: Application à la dispersion de polluants (phdthesis, Université de la Réunion). Retrieved from https://theses.hal.science/tel-00633096

Lesouëf, D., Gheusi, F., Delmas, R., & Escobar, J. (2011). Numerical simulations of local circulations and pollution transport over Reunion Island. *Annales Geophysicae*, *29*(1), 53–69. https://doi.org/10.5194/angeo-29-53-2011

Lunet, T., Lac, C., Auguste, F., Visentin, F., Masson, V., & Escobar, J. (2017). Combination of WENO and explicit Runge–Kutta methods for Wind transport in the Meso-NH model. *Monthly Weather Review*, *145*(9), 3817–3838. https://doi.org/10.1175/MWR-D-16-0343.1

Manins, P. C., & Sawford, B. L. (1979). A model of katabatic winds. *Journal of the Atmospheric Sciences*, *36*(4), 619–630. https://doi.org/10.1175/1520-0469(1979)036⟨0619:AMOKW⟩2.0.CO;2

Masson, V., Le Moigne, P., Martin, E., Faroux, S., Alias, A., Alkama, R., et al. (2013). The SURFEXv7.2 land and ocean surface platform for coupled or offline simulation of Earth surface variables and fluxes. *Geoscientific Model Development*, *6*(4), 929–960. https://doi.org/10.5194/gmd-6-929-2013

Nadeau, D. F., Pardyjak, E. R., Higgins, C. W., Huwald, H., & Parlange, M. B. (2013). Flow during the evening transition over steep Alpine slopes. *Quarterly Journal of the Royal METEOROLOGICAL Society*, *139*(672), 607–624. https://doi.org/10.1002/qj.1985

Noilhan, J., & Planton, S. (1989). A simple parameterization of land surface processes for meteorological models. *Monthly Weather Review*, *117*(3), 536–549. https://doi.org/10.1175/1520-0493(1989)117⟨0536:ASPOLS⟩2.0.CO;2

Randall, D. A., Dazlich, D. A., Zhang, C., Denning, A. S., Sellers, P. J., Tucker, C. J., et al. (1996). A revised land Surface Parameterization (SiB2) for GCMS. Part III: The greening of the Colorado State University general circulation model. *Journal of Climate*, *9*(4), 738–763. https://doi.org/10.1175/1520-0442(1996)009⟨0738:ARLSPF⟩2.0.CO;2

Réchou, A., Flores, O., Jumaux, G., Duflot, V., Bousquet, O., Pouppeville, C., & Bonnardot, F. (2019). Spatio-temporal variability of rainfall in a high tropical island: Patterns and large-scale drivers in Réunion Island. *Quarterly Journal of the Royal Meteorological Society*, *145*(720), 893–909. https://doi.org/10.1002/qj.3485

Rocco, M., Baray, J., Colomb, A., Borbon, A., Dominutti, P., Tulet, P., et al. (2022). High resolution dynamical analysis of Volatile Organic Compounds (VOC) measurements during the BIO-MAÏDO field campaign (Réunion Island, Indian ocean). *Journal of Geophysical Research: Atmospheres*, *127*(4), e2021JD035570. https://doi.org/10.1029/2021JD035570

Rucker, M., Banta, R. M., & Steyn, D. G. (2008). Along-Valley structure of daytime thermally driven flows in the Wipp valley. *Journal of Applied Meteorology and Climatology*, *47*(3), 733–751. https://doi.org/10.1175/2007JAMC1319.1

Sabatier, T., Paci, A., Lac, C., Canut, G., Largeron, Y., & Masson, V. (2020). Semi-idealized simulations of wintertime flows and pollutant transport in an Alpine valley: Origins of local circulations (Part I). *Quarterly Journal of the Royal Meteorological Society*, *146*(727), 807–826. https://doi.org/10.1002/qj.3727

Sturman, A. P., & McGowan, H. A. (1995). An assessment of boundary-layer air mass characteristics associated with topographically-induced local wind systems. *Boundary-Layer Meteorology*, *74*(1–2), 181–193. https://doi.org/10.1007/BF00715716

Tian, Y., & Miao, J. (2019). A numerical study of mountain-plain breeze circulation in Eastern Chengdu, China. *Sustainability*, *11*(10), 2821. https://doi.org/10.3390/su11102821

Tulet, P., Di Muro, A., Colomb, A., Denjean, C., Duflot, V., Arellano, S., et al. (2017). First results of the Piton de la Fournaise STRAP 2015 experiment: Multidisciplinary tracking of a volcanic gas and aerosol plume. *Atmospheric Chemistry and Physics*, *17*(8), 5355–5378. https://doi.org/10.5194/acp-17-5355-2017

Vié, B., Pinty, J.-P., Berthet, S., & Leriche, M. (2016). LIMA (v1.0): A quasi two-moment microphysical scheme driven by a multimodal population of cloud condensation and ice freezing nuclei. *Geoscientific Model Development*, *9*(2), 567–586. https://doi.org/10.5194/gmd-9-567-2016

Wang, C.-C., & Kirshbaum, D. J. (2015). Thermally forced convection over a mountainous tropical island. *Journal of the Atmospheric Sciences*, *72*(6), 2484–2506. https://doi.org/10.1175/jas-d-14-0325.1

Weinkaemmerer, J., Ďurán, I. B., & Schmidli, J. (2022). The impact of large-scale winds on boundary layer structure, thermally driven flows, and exchange processes over mountainous terrain. *Journal of the Atmospheric Sciences*, *79*(10), 2685–2701. https://doi.org/10.1175/JAS-D-21-0195.1

Yang, Y., Chen, Y.-L., & Fujioka, F. M. (2005). Numerical simulations of the Island-induced circulations over the island of Hawaii during harp. *Monthly Weather Review*, *133*(12), 3693–3713. https://doi.org/10.1175/mwr3053.1

Zardi, D., & Whiteman, C. (2013). Diurnal Mountain wind systems. *Mountain Weather Research and Forecasting*, 35–119. https://doi.org/10.1007/978-94-007-4098-3_2